City Research Online

City St George's, University of London

Citation: Khan, K., Chen, Z., Liu, J. & Tsavdaridis, K. D. (2023). Compressive behaviors of corner-supported modular steel sway frames with rotary inter-modular connections. Thin-Walled Structures, 193, 111245. doi: 10.1016/j.tws.2023.111245

This is the accepted version of the paper.

This version of the publication may differ from the final published version. To cite this item please consult the publisher's version.

Permanent repository link: https://openaccess.city.ac.uk/id/eprint/31773/

Link to published version: https://doi.org/10.1016/j.tws.2023.111245

Copyright and Reuse: Copyright and Moral Rights remain with the author(s) and/or copyright holders. Copies of full items can be used for personal research or study, educational, or not-for-profit purposes without prior permission or charge, unless otherwise indicated, provided that the authors, title and full bibliographic details are credited, a hyperlink and/or URL is given for the original metadata page and the content is not changed in any way. For full details of reuse please refer to City Research Online policy.

City Research Online: http://openaccess.city.ac.uk/ publications@citystgeorges.ac.uk

Compressive behaviors of corner-supported modular steel sway frames with rotary inter-modular connections

Kashan Khan[a], Zhihua Chen[a,b,c], Jiadi Liu[a], Konstantinos Daniel Tsavdaridis[d]
[a] *Department of Civil Engineering, Tianjin University, Tianjin, China*
[b] *State Key Laboratory of Hydraulic Engineering Simulation and Safety, Tianjin, China*
[c] *Key Laboratory of Coast Civil Structure and Safety, Tianjin University, Tianjin, China*
[d] *Department of Engineering, School of Science & Technology, City, University of London, Northampton Square, EC1V 0HB, London, UK*

Abstract: Corner-supported modular steel sway frames (CMSFs) with rotary inter-modular connections (IMCs) differed from traditional frames regarding their column discontinuities, beam groupings, and unique intra- and inter-modular connections, necessitating the investigation into their compressive performance to guarantee their safe and reliable application. This study investigated the compressive behavior of CMSFs with rotary IMCs using experimental tests, numerical modeling, and theoretical analysis. Three compression tests were conducted on sub-assembled CMSFs, considering varying floor and ceiling beam stiffnesses. The results showed that all frames experienced lateral sway, with upper columns at lower regions undergoing inward or outward elastic and plastic local buckling. RS1 (RS2) demonstrated 12% (3%) higher strength than RS3, and stiffness increased by 2% for RS1 compared to RS3. Pre- and post-ultimate ductility of RS3 was 3% (13%) and 20% (37%) greater than RS1 (RS2), indicating that increased rigidity with thicker beams enhanced strength and stiffness but resulted in reduced CMSFs' ductility. A finite element model (FEM) was generated, and its accuracy was verified using experimental load-shortening and failure outcomes, revealing an average prediction error of 0.3%, 9.1%, and 8.5% for compressive resistance, stiffness, and ductility index, respectively. Based on validated FEMs, a parametric study was conducted on 77 CMSFs to investigate the effects of varying beam and column sizes, lengths, beam gaps, and connecting plate thicknesses on compressive resistance, stiffness, and pre-and post-ultimate ductilities. Increasing

column and beam sizes from 150 to 200 mm and thicknesses from 6 to 8 mm enhanced strength and stiffness by up to 123% (55%) and 46% (10%), with pre-and post-ultimate ductility growing by 16% (113%) and 15% (19%). However, lengthening them from 0.6 to 1.2 and 3 m decreased CMSFs' strength (stiffness) by up to 37% (5%) and 65% (71%), with no IMC failure. The sub-assembled CMSFs' buckling load was evaluated using theoretical models, considering members' stiffnesses and rotary IMC as pinned and semi-rigid. The average theory-to-FEM buckling load for pinned and semi-rigid IMC was 0.70 and 0.96, indicating that both models were conservative. However, considering IMC's rotational stiffness provided less scattering and a more realistic depiction of the CMSFs' buckling behavior than the pinned model. The study's findings and the accuracy of theoretical buckling models ensured they could conservatively design CMSFs under compressive loadings while considering their uniquenesses.

Keywords: Compressive behaviors; Rotary inter-modular connections; Corner-supported modular steel sway frames; Sub-assembled frame testing; Finite element parametric analysis; Theoretical buckling load models

1 Introduction

Modular steel buildings (MSBs) utilize prefabricated modules interconnected with inter-modular connections (IMCs) to create efficient, high-quality, safe, and eco-friendly structures [1,2]. They have emerged as successful alternatives to traditional steel buildings (TSBs) for various projects, such as COVID-19 hospitals [3], 29-story SOHO and Apex [4], and 32-story B2 towers [5]. The assembly, structural stability, and performance of MSBs rely significantly on intra- and inter-modular connections. Beam-column intra-modular connections are typically welded joints due to their higher capacity than fin-plate or bolted connections [2]. Meanwhile, IMCs transmit forces between modules [6]. Considerable investigation has been carried out on IMC designs and their mechanical performance under various loading conditions, leading to a comprehensive understanding of their advantages and limitations [4,5,7–11].

Corner-supported modular steel units in MSBs provide a distinct load transfer path and superior offsite prefabrication compared to other modules [12,13]. Corner-supported modular steel sway frames (CMSFs), or non-sway frames, have been the primary focus of IMC research, with CMSFs capable of replicating nonlinear *P*-Delta effects, leading to significant bending moments in intra- and inter-modular connections and distinct structural responses compared to non-sway frames [14]. Extensive research has been conducted on tensile [15–18], shear [17,19–24], bending [21,25,26], and seismic performance [16,27–35] of welded [36–40], bolted [2,26,27,41–47], shear-keyed [24,29,54–63,34,64–71,35,48–53], pre- and post-tensioned [19,20,25,28,31,67,72,73], and automatic [16,18,23,30,50,74–76] IMCs. Depending on load capacity, resilience, installation convenience, and disassembly, each IMC type has pros and cons. For instance, welded IMCs are durable but susceptible to weld fractures or stress concentration [28]. Bolted IMCs are ductile but less resilient than welded joints and

require member openings, making them prone to gradual loosening or failure [7]. Shear-keyed IMCs are stiff and effective against lateral loads, but they can cause column shear stresses and require careful installation [51,77]. Pre- and post-tensioned IMCs are strong but may experience tension relaxation issues over time and require specialized equipment and expertise for installation [7,17]. Automatic IMCs are resilient and self-tightening but require high precision and are complex to install [30]. Besides, the low rotational stiffness of welded or cover-plate bolted IMCs hinders them from being used in high-rise MSB or earthquake-prone regions [33]. The inability to disassemble these IMCs prevents MSB reuse [15]. Rotary IMC eliminates the need for on-site welding or member opening, allowing for fast disassembly and the choice of alternative cross-sectional forms [2,17,26,41,42,78]. The complex design of rotary IMC demands specialized skills for precise alignment and compatibility with other modules, as well as load distribution, durability, and compliance with existing structures and design standards, all of which can affect the compressive behavior, stiffness, capacity, and ductility of the CMSFs depicted in **Figs. 1 and 2**. Understanding these factors is crucial for delivering secure and sustainable MSBs [2,26,41,42].

Despite extensive research on MSBs under various loads, existing practices, such as alignment charts [79] and simplified equations [80], may not accurately apply to the compressive design of CMSFs due to the semi-rigidity of IMCs, distinguishing them from regular frame systems in TSBs [81]. In MSBs, IMCs generate discontinuities and groupings of columns, beams, and IMCs, unlike traditional continuous columns attached to beams [82–84]. This distinction can lead to non-conservative or excessively conservative designs, posing stability risks for MSBs [85]. While conventional columns have been extensively studied, the compressive behavior of MSBs requires more attention. Some compressive tests on multi-column walls assumed homogeneous load

distribution and neglected the impact of adjacent modular units, IMCs, and complex joint zones [86–90]. Other studies developed theoretical buckling load models for the conservative design of single and grouped columns with shear-keyed IMCs but did not consider IMCs between adjacent modules [58,63,77,91,92]. A simplified analysis approach to compute column buckling length was proposed by Zhang [93], but its applicability to multi-story MSB columns is unclear. Several focused on stubs or non-sway braced frames with specialized members or IMCs [15,91,92,94–96], but they did not account for the secondary moment effect, limiting their practicality for standard MSBs [97]. Sway and non-sway frames with corner IMCs have been examined by Li et al. [98,99], Farajian et al. [81], Zhai et al. [100], and Wang and Su [101], providing alignment charts for columns *K*-factors and simplified formulas following French rules [102]. However, these studies lacked experimental support for specific types of IMCs, ignored the rotational stiffness of vertical and horizontal IMCs and joint design, and relied on limited data for fitting, necessitating more precise and straightforward methodologies [100]. Moreover, some studies classified connections' strength and stiffness responses, gave design recommendations, and validated proposed systems, but they disregarded nonlinear analyses and structural post-buckling behavior under multiple limit states [103–105]. Since simplified connections and models cannot accurately determine the structural mechanism, MSB buckling length, and load calculations, they may produce inappropriate values [106]. Assuming rotary IMCs to be either pinned [38,107,108] or rigid [109] in CMSFs, like those used in TSBs [110,111], could lead to inaccurate predictions of the compressive response [15].

A comprehensive examination of the compressive behavior of CMSFs considering the *P*-Delta effect, the relative stiffness of module members and IMCs was needed to develop accurate finite element models (FEMs) for replicating the actual behavior of

CMSFs [2,9,82–84,112]. Such analyses were required to focus on the nonlinear behavior of CMSFs. Thus, compressive testing, accurate modeling, analysis, and design were necessary to conservatively evaluate buckling load from semi-rigid to pinned boundaries, eliminating the need for charts to address the shortcomings and ensure the stability, integrity, and resilience of MSBs. Considering the compressive performance of these systems, specific types of IMCs [14], and the stability-relevant mechanical properties of IMCs [2], global stability and reliable design approaches needed to be investigated [106]. The objective of the current study was to contribute to this area by exploring the compressive behavior of CMSFs using rotary IMCs, as outlined in [26]. Three subassemblies representing framed exterior modules resembling sway frames were tested under compressive load [14]. Validated FEMs were used to evaluate the effects of parameter variation. The experimental and FEM results corroborated theoretical models assuming semi-rigid and pinned IMCs, enabling conservative predictions of the buckling loads of sub-assembled CMSFs and facilitating the design of cost-effective, secure, and sustainable MSBs.

Fig. 1 Application of CMSFs with rotary IMC patent [113] in authors' designed MSB [114]

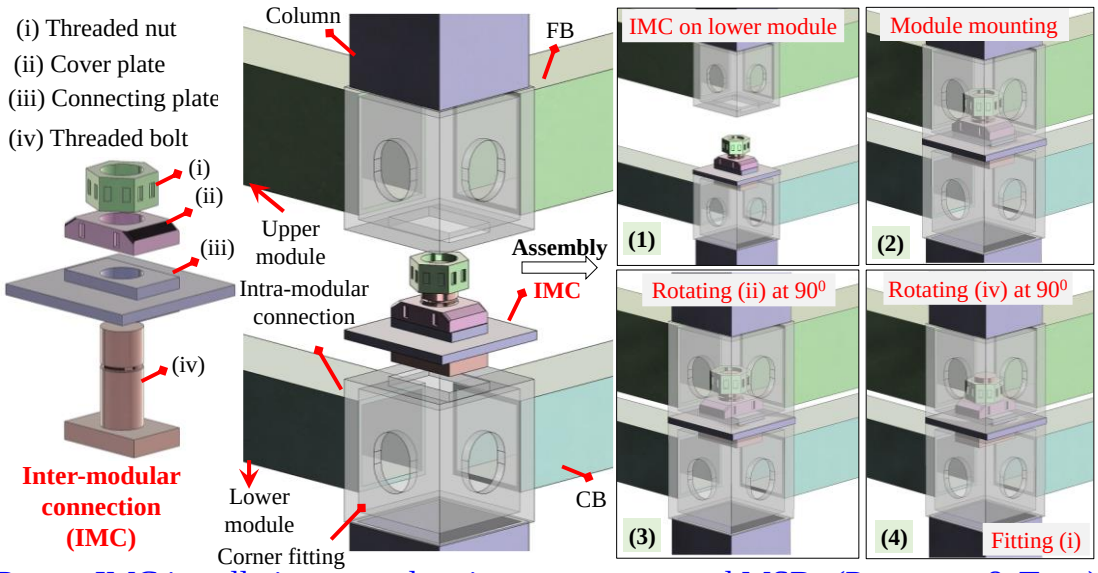

Fig. 2 Schematic diagram of assembling of CMSF with rotary IMC (IMC's components design details and specifics based on [2,26,41,42,78])

2 Compression tests on CMSFs with rotary IMCs

Compressive testing of sub-assembled CMSFs with rotary IMCs replicated the exterior sway frame, examining critical compression stresses that cause stability loss and initiate buckling.

2.1 Specimens design

Fig. 1 showed the application of rotary IMC modules in 5-story Ziya Shanglinyuan MSBs with dimensions of 8.5×3.0×3.0 m and 6.7×3.0×3.0 m [2,17,26,41,42,78] per GB50017-2017 [115], serving as a prototype for this study's engineering context and IMC designs. The IMC consisted of four components: a threaded nut, cover plate, connecting plate, and threaded bolt, whose installation procedures were depicted in **Fig. 2**. To examine compressive behavior and failure response in CMSFs, three sub-assembled exterior frames were designed, each incorporating unique roller supports on beam ends [14]. The objective of the testing was to gather empirical data for FEM validation, followed by parametric and theoretical research to develop buckling load models that incorporate rotary IMCs. The current study adopted sub-assembled specimens, so the outcomes were related to those in full-frame [14,16,28–31,116]. The

lengths of columns and beams were determined using mid-length inflection points, which comprised half of their total lengths. While the semi-rigid behavior of rotary IMCs could affect the CMSF's inflection point, the specimen's design employed simplified pinned-ended assumptions, ignoring IMC rotational rigidity to achieve conservative results by underestimating capacity and stiffness. This offered a comprehensive understanding of the relationship between assumptions and actual behavior, highlighting the significance of joint rigidity when analyzing the compressive behavior of CMSF [14]. The welding seam for the columns and beams was located in the middle of the section, resulting in a butt joint created with groove welding. Following the prototype project, a 74 mm gap was maintained between floor beams (FBs) and ceiling beams (CBs) to allow for services [14].

2.2 Specimens geometry

Fig. 3(a,b) and **Table 1** presented specimen geometry and component design details, while the IMC components' design details were from previous works [2,26,41,42,78], as depicted in **Fig. 3(c)**. Due to the primary load-bearing member, the flexural stiffness of FBs was maintained higher than that of CBs; therefore, the cross-sectional depth of FBs (B_{FB}) was greater than that of CBs (B_{CB}). RS1 selected a thicker FB than CB, whereas RS2 and RS3 selected similar thicknesses [116]. The thickness of the ceiling beam (t_{CB}) was increased to 8 mm in RS2, and the thickness of the floor beam (t_{FB}) was decreased to 6 mm in RS3 relative to RS1. Various t_{FB} and t_{CB} were considered to examine the effect of beam and intra-modular connections on the compressive behaviors of CMSFs. All specimens were prepared with identical heights and widths of 3375 and 1568 mm while maintaining the clear height and length of the upper and lower columns (L_c) at 1266 mm, and the floor (L_{FB}) and ceiling (L_{CB}) beams at 1192 mm. Adopted was the same 200×200×8 mm column measuring 200 mm in length (D_c), 200

mm in width (B_c), and 8 mm in thickness (t_c). Cross-section width (D_{FB}) and depth (B_{FB}) of 150 and 200 mm for FBs and width (D_{CB}) and depth (B_{CB}) of 150 mm for CBs were selected. Meanwhile, members' cross-section sizes, columns height, and beam lengths (L_c, L_{FB}, and L_{CB}) were maintained.

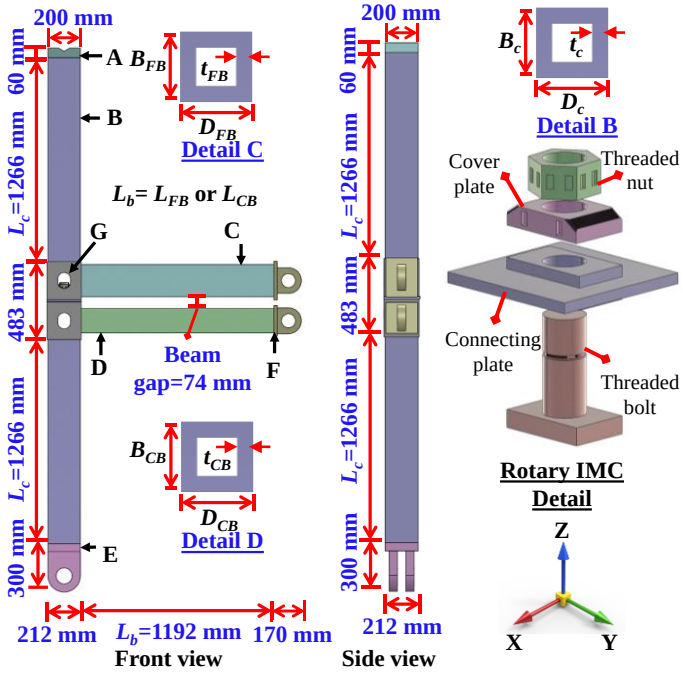

(a) Specimen details of CMSF with rotary IMC

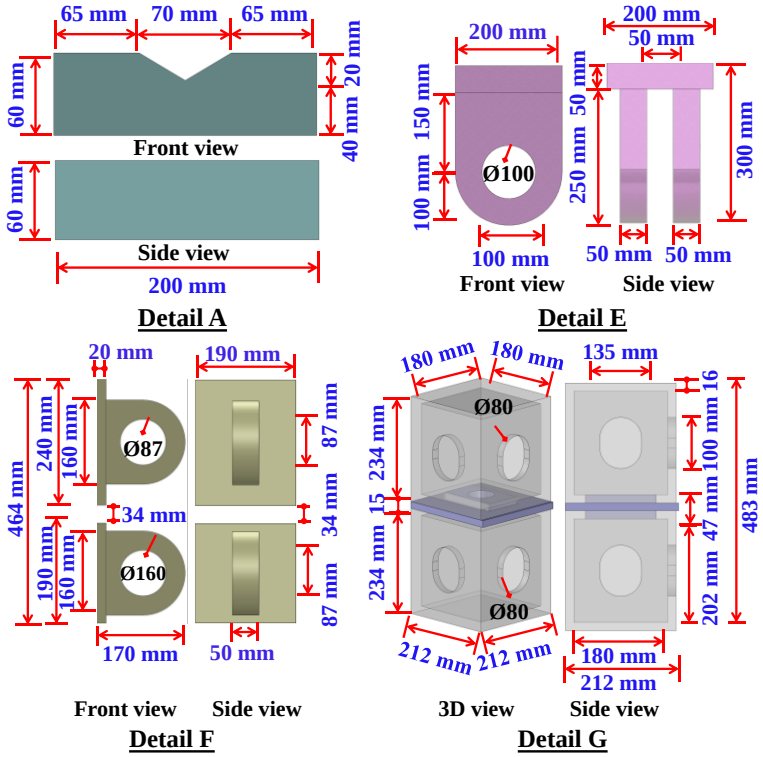

(b) Details of the selected components

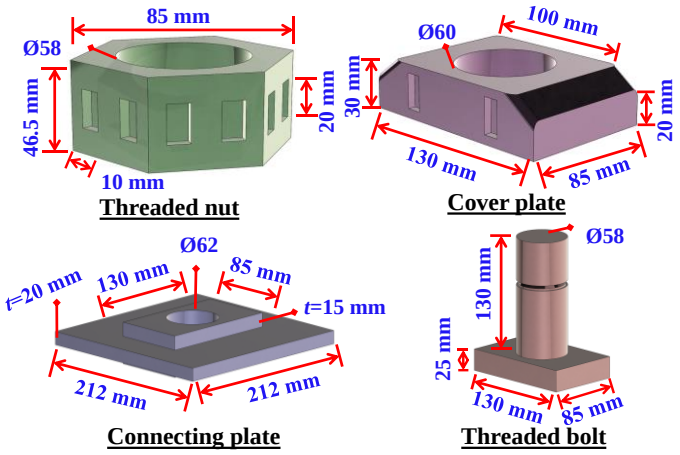

(c) Rotary IMC's components design details

Fig. 3 Details of tested sub-assembled CMSFs with rotary IMCs

2.3 Material properties

GB/T228.1-2010 [117] was used to design steel coupons from the same material to analyze test results and generate FEM. Thickness measurements of 15 coupons, three for each of the five cross-sectional sizes of members, showed variations that notably affected strength, ductility, failure modes, and yield plateau, while stiffness remained constant. The mean values of the obtained parameters and thicknesses are detailed in **Table 1**. Additionally, **Fig. 4(a~f)** illustrates the test setup, failure modes, and tensile stress-strain curves of the coupons.

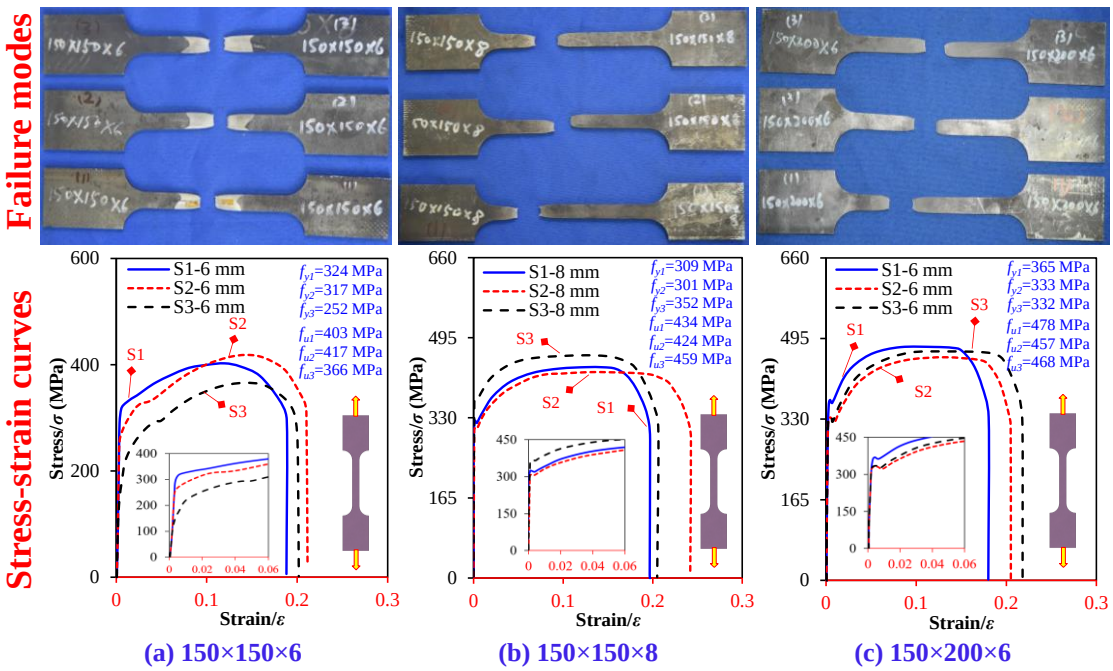

(a) 150×150×6 **(b) 150×150×8** **(c) 150×200×6**

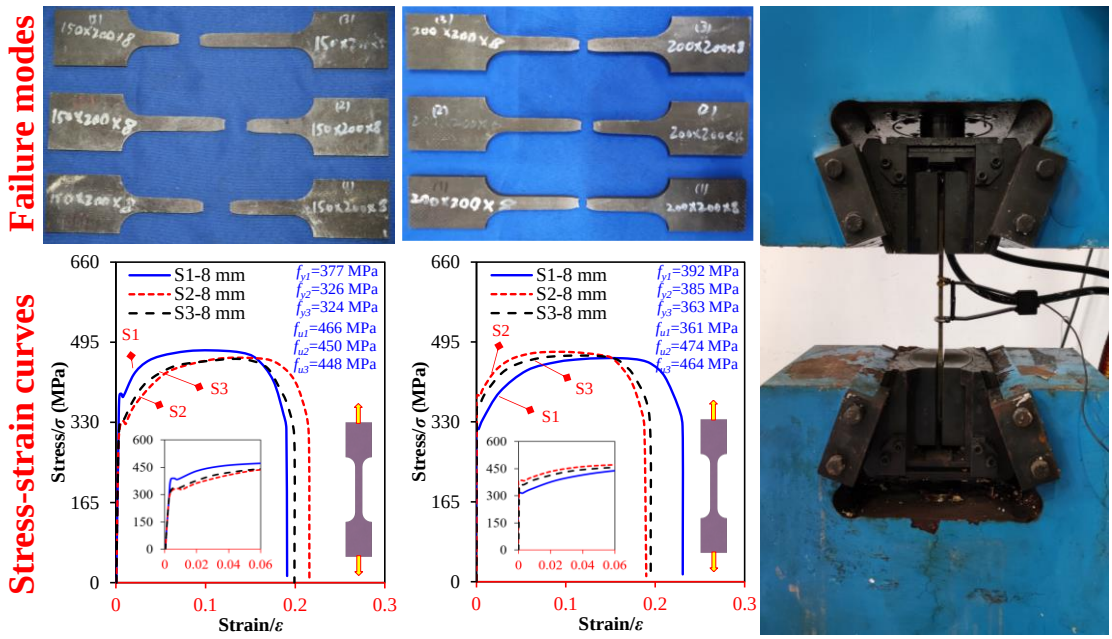

(d) 150×200×8 (e) 200×200×8 (f) Testing setup

Fig. 4 Coupons' tensile testings outcomes

2.4 Test setup

Fig. 5(a,b) depicts the CMSF's compression testing setup. The specimens' upper and lower frame skeletons were connected with rotary IMC on the ground, as illustrated in **Fig. 2**, before being mounted on the setup following [2,17,26,41,42,78]. A 300*t* vertical hydraulic jack applied compressive force to the upper columns. Column roller supports were positioned above the jack to facilitate lateral movement of the jack and specimen, maintaining compressive force even during specimen shortening and lateral deflection. The jack's base was secured to a load sensor using a plate and threaded bolts to record reaction forces. The load sensor's top and bottom ends were anchored with a jack and knife-edge support through threaded bolts welded onto plates. The knife-edge support was welded to the bottom end of the plate to maintain flat support, transferring load instantly to the upper column while allowing rotation. This support enabled in-plane rotation while restricting out-of-plane rotation. On the ends of beams, roller supports were devised and installed to limit vertical translation while allowing lateral translation and in-plane rotation. At the lower column's base, a pin cell provided hinged support,

preventing in- and out-of-plane translation while allowing in-plane rotation. As a standard for column-end loadings, a similar testing technique was recommended in [14], as seen in [2,28,29,31,34,41,42,78,118]. A laser level was used to verify the specimen and load setup's straightness. Afterward, the jack was slightly pressed to maintain vertical alignment, measuring devices were attached, and formal testing was initiated.

The loading was subdivided into preloading and formal loading, as per GB/T50344-2019 [119]. The measuring devices' accuracy was confirmed by applying a $0.2P_u$ (CMSF's ultimate compressive resistance) preload. Specimens were held for two minutes after reaching preload before being completely unloaded for another two minutes, as depicted in **Fig. 5(c)** [120,121]. A combination of force and displacement-controlled loadings was adopted, suitable for structures with unpredictable yield displacements [122]. After a force loading till yielding, displacement loading of 0.05 mm/min was used until it dropped to 85% of P_u [123]. Once the load-shortening curves entered the nonlinear phase, displacement loading was initiated, determined by reaction forces registered by the load sensor and vertical shortening by LVDT.

Strain gauges assess deformation and force transfer mechanisms [124]. As depicted in **Fig. 6(a~c)**, strain gauges were mounted on upper columns (UCs), lower columns (LCs), FBs, CBs, and upper and lower corner fittings to evaluate local elastic or plastic buckling if it happened before or after material's yield [125]. At least one strain gauge was placed in potentially buckling-prone locations to ensure accurate assessment. Columns were susceptible to in- and out-of-plane local buckling near IMC; strain gauges on columns and corner fittings were positioned vertically along the height. Beams were allowed to rotate, and due to significant stress near the intra- and inter-modular connections, strain gauges were placed up to 200 mm. While the FB and CB gap was small for working, no strain gauge was employed there. On RS1, there were

47, while on RS2 and RS3, there were 56 strain gauges. As illustrated in **Fig. 6(d)**, eight horizontal linear variable differential transducers (LVDTs) were positioned vertically on LCs, UCs, and corner fittings identified by H1-H8 to measure the degree of lateral deflection, translation, sway, or buckling. A vertical LVDT V3 was mounted on a jack-fixed knife-edge support to assess the specimens' end-shortening. Similarly, V1 and V2 measured the vertical deflection of CBs and FBs near IMC.

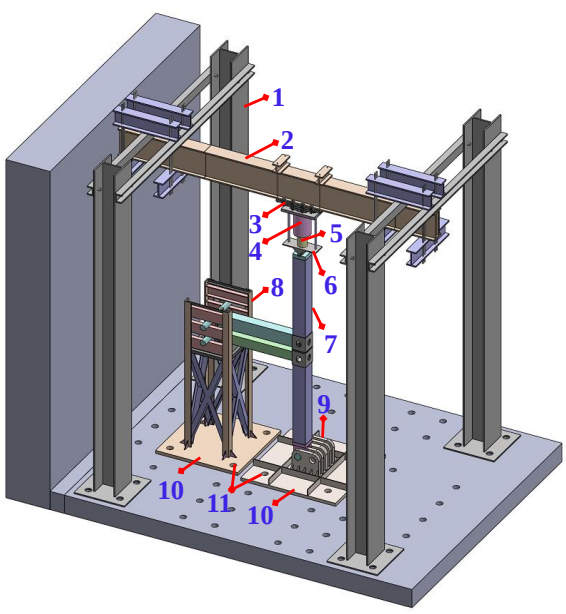

(a) Test setup schematic diagram

(b) Test setup and specimen before the test

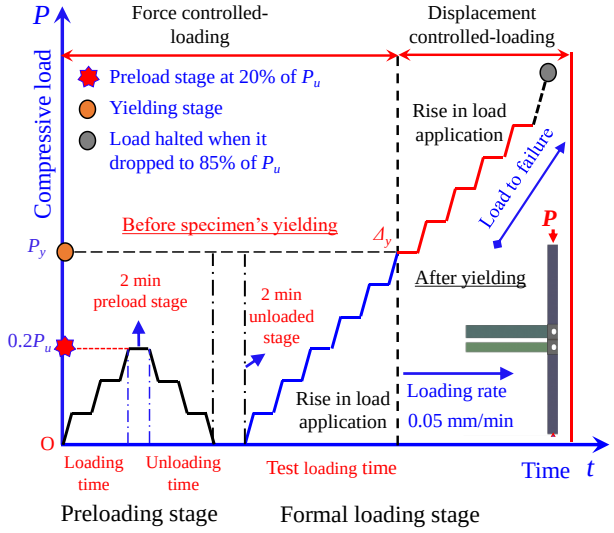

(c) Loading protocol

Fig. 5 Generalized compression testing setup of sub-assembled CMSFs with rotary IMCs. (1-Reaction frame; 2-Reaction beam; 3-Column roller support; 4; Vertical hydraulic jack; 5-Load sensor; 6-Knife-edge support; 7; CMSFs specimen with rotary IMCs; 8-Beams roller support; 9-Hinged support; 10-Pedestal; 11-Anchor bolt holes)

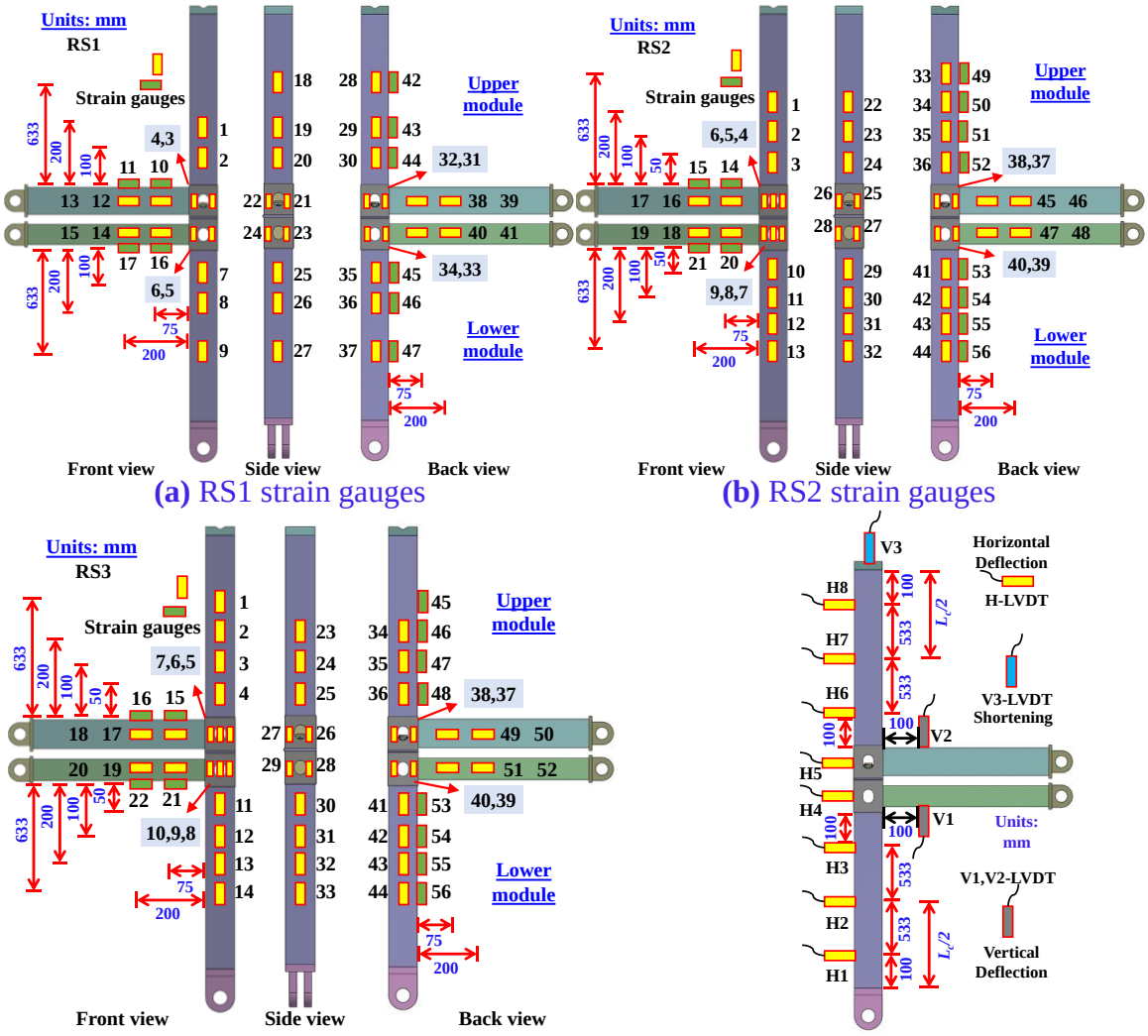

(a) RS1 strain gauges **(b)** RS2 strain gauges

(c) RS3 strain gauges **(d)** RS1, RS2, and RS3 LVDTs

Fig. 6 Detailed location of strain gauges and LVDTs on CMSFs

3 Experiment outcomes

3.1 Failure modes

Fig. 7(a~c) demonstrates the CMSF failure mechanisms detected in RS1, RS2, and RS3. As the lateral sway (Δ_c) indicated, all CMSFs exhibited in-plane translation, controlled by the horizontal translation of floor and ceiling beams, leading to frame instability in the same direction. While all CMSFs experienced the same failure, RS1 and RS3 swayed in the direction of beams due to thinner beams compared to columns, but RS2 exhibited failure in the opposite direction because beams and columns had the same thickness, preventing significant movement towards the beams. The CMSFs displayed distinct translations when subjected to compressive loads, particularly in the FBs and

CBs. As the applied load increased, lateral translation became more pronounced. While both beams moved in the same direction, there were noticeable variations, especially in the deflection of FBs. For instance, the deflection of FBs increased by 12% in RS1, 16% in RS2, and 15% in RS3. This indicates a significant increase in the in-plane translation of the CMSFs, especially with local column buckling. Additionally, the CB and FB translations were measured at nearly 16 mm and 18 mm in RS1, but these decreased by 33% and 31% in RS2 and increased to 79% and 81% for RS3. This suggests that the beams in RS3 demonstrated a more pronounced lateral movement than those in RS1 and RS2, highlighting the significant influence of the beams' flexural rigidity on the failure position by affecting stress propagation, translation, and rotation. Moreover, non-rigid constraints permitted the upper and lower frame skeleton's slight gapping and rotation around the IMC. When local buckling occurred in the UC, the CMSF suffered an abrupt rise in in-plane translation. Because the CMSF could not sustain or transfer additional loads after buckling, the loading was halted for safety concerns. Local inward and outward buckling (IB/OB) at the base of the UC towards the IMC was the primary cause of failure. It occurred at a distance of 50-100 mm for RS1 and RS2 while 50-200 mm for RS3 from the edge of the corner fitting, confirmed by the greater strain values in the UCs' lower regions. Buckling on the UCs bending side was more apparent than on the opposite. Similar failure modes and their concentration on column faces adjacent to column bending sides supported the absence of out-of-plane translation and rotation, indicating compressive behavior was controlled in-plane. Rotary IMC transmitted force to other members without localized failure, ensuring CMSF's safety and integrity. As shown in **Fig. 11(a~c)**, comparing yield strain showed no location on beams or corner fittings yielded or buckled before achieving CMSF's ultimate compressive resistance. Similarly, most regions on the LCs did not yield; however, several areas on the UCs

292 did yield, indicating that the upper column was the primary load carrier. Except for
293 portions in or opposite bending directions revealing local elastic buckling, other regions
294 of UCs exhibited local plastic buckling in CMSFs.

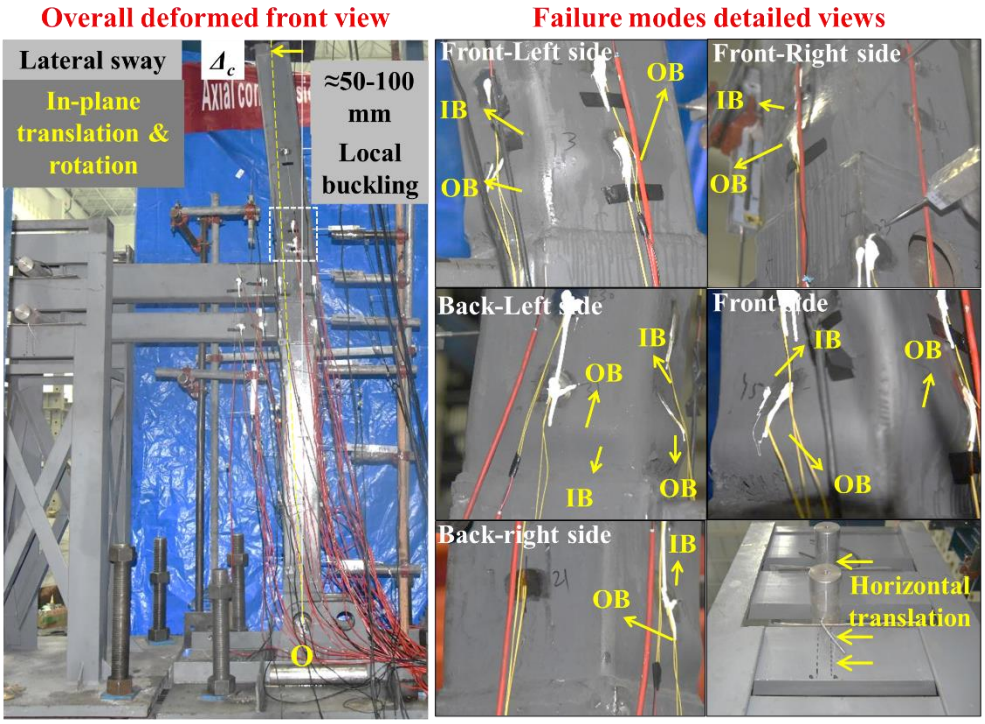

295 **(a) RS1 specimen**

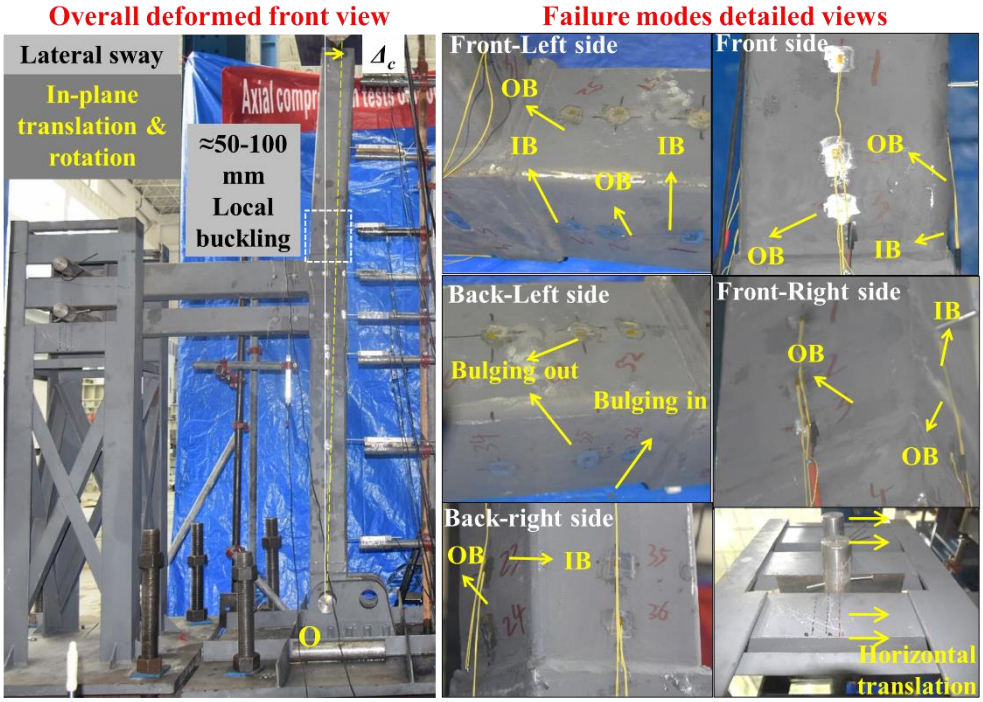

296 **(b) RS2 specimen**

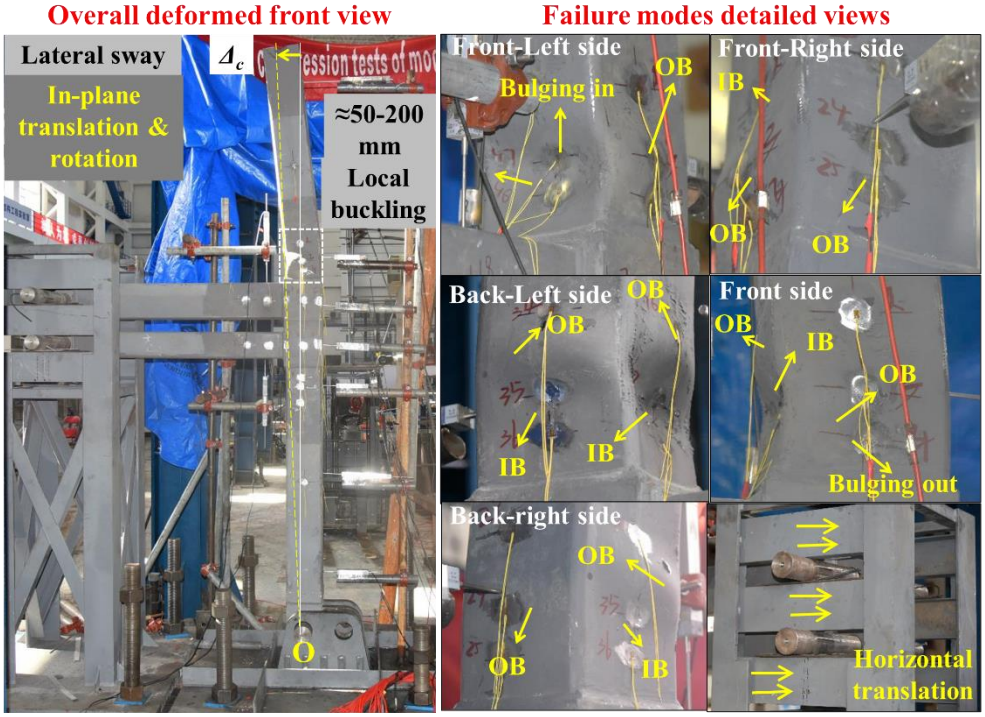

297
298 **Fig. 7** Failure modes of CMSF under compression (IB/OB, inward/outward buckling)

Table 1 Design details and comparison of compression tests and FEMs of CMSFs with rotary IMC

Item	D_{FB} (mm)	B_{FB} (mm)	t_{FB} (mm)	L_{FB} (m)	D_{CB} (mm)	B_{CB} (mm)	t_{CB} (mm)	L_{CB} (m)	$P_{u,Test}$ (kN)	$K_{e,Test}$ (kN/mm)	$\Delta_{u,Test}$ (mm)	DI_{Test} (Ratio)
RS1	150	200	8	1.2	150	150	6	1.2	1397	343	6.1	1.8
RS2	150	200	8	1.2	150	150	8	1.2	1279	321	5.4	1.4
RS3	150	200	6	1.2	150	150	6	1.2	1244	339	6.2	2.3

Item	$P_{u,Test}$ (kN)	$P_{u,FE}$ (kN)	$\frac{P_{u,Test}}{P_{u,FE}}$	$K_{e,Test}$ (kN/mm)	$K_{e,FE}$ (kN/mm)	$\frac{K_{e,Test}}{K_{e,Test}}$	$\Delta_{u,Test}$ (mm)	$\Delta_{u,FE}$ (mm)	$\frac{\Delta_{u,Test}}{\Delta_{u,FE}}$	DI_{Test} (Ratio)	DI_{FE} (Ratio)	$\frac{DI_{Test}}{DI_{FE}}$
RS1	1397	1403	1.00	343	413	0.83	6.1	4.0	1.53	1.8	2.0	0.94
RS2	1279	1256	1.02	321	342	0.94	5.4	4.6	1.17	1.4	2.0	0.70
RS3	1244	1251	0.99	339	354	0.96	6.2	4.6	1.34	2.3	2.1	1.10
Mean			1.00			0.91			1.35			0.91
Cov			0.01			0.06			0.11			0.18

Item	Length (mm)	Width (mm)	Thickness (mm)	f_y (MPa)	f_u (MPa)	δ (%)	E_s (GPa)
Beam-1	150	150	6(5.37)	298	395	22.2	201
Beam-2	150	150	8(7.33)	321	439	23.6	209
Beam-3	150	200	6(5.54)	344	468	24.9	208
Beam-4	150	200	8(7.30)	342	455	23.5	210
Column	200	200	8(7.34)	380	434	22.7	206
Corner fittings[1]	-	-	16(15.80)	351	518	23.0	198
IMC (ii, iii)[1]	-	-	-	360	580	34.0	206
IMC (i, iv)[1]	-	-	-	360	610	16.0	206

D_{FB}, B_{FB}, t_{FB}, L_{FB}; D_{CB}, B_{CB}, t_{CB}, L_{CB}; $P_{u,\,Test}$ ($P_{u,\,FE}$), $K_{e,\,Test}$ ($K_{e,\,FE}$), $\Delta_{u,\,Test}$ ($\Delta_{u,\,FE}$), DI_{Test} (DI_{FE}); and f_y, f_u, δ, E_s represent the floor and ceiling beam's width, depth, thickness, length; ultimate compressive resistance, initial stiffness, ultimate shortening, post-ultimate ductility index via test (FEM); material yield strength, ultimate strength, percentage elongation, elastic modulus—Note:[1] Material properties obtained from [2]. The thickness values in the bracket represent the average measured thickness.

3.2 Load-shortening curves

Fig. 17(a~c) demonstrates the CMSFs' load-shortening (P-Δ) curves, while **Fig. 17(f)** shows their generalized behavior, implying that all illustrations displayed elastic (I), inelastic (II), and recession (III). *'P'* represents the compressive load, while *'Δ'* indicates the shortening. The recession is a stage after the ultimate stage defined by a succeeding trough with a sharp decline in the load-carrying capacity that may extend to larger shortening [126–132]. These curves determine P_u, ultimate shortening (Δ_u), initial stiffness (K_e), and ductility index (DI) [133,134]. The load grows linearly with shortening during stage I until the yield strength (P_y) is achieved. At the transition, the increase in capacity is characterized by a decrease in the stiffness of curves because of exceeding the bending stresses at UCs' multiple locations. During stage II, from P_y until P_u, the curves acquire a parabolic shape; concurrently, local buckling appears on the UCs as an inward and outward pattern as the bending and P-Delta effect intensifies. RS1 (RS2)'s P_u values are 12% (3%) higher than RS3. Compared to RS3, K_e shows marginal fluctuation by rising to 2% for RS1. It indicates that increased rigidity with thicker beams enhances strength and stiffness. Meantime, as determined by strain values, local elastic buckling is found mainly in the bending direction, owing to bending stresses and P-Delta effects that appear to reduce column stiffness relative to other sides. Δ_u of RS3 is 3% (13%) greater than RS1 (RS2) due to the thinner beams, with RS2 having the lowest value due to the thickest beams. Thicker beams reduce buckling strain and premature instability, diminishing CMSFs' ductility. Stage III is marked by decreased capacity, sharp deflection increase, and severe local buckling. Similarly, the DI can be compared at the post-ultimate stage. The DI represents the capacity of frame columns to undergo plastic deformation beyond the ultimate load, providing insight into their post-peak deformation capacity, structural stability, and the potential for

design improvements and strengthening techniques [77,91,92,123,133]. RS3 has more excellent post-ultimate ductility of 20% (37%) and a better recession stage than RS1 (RS2), indicating that stiffer beams enable plastic deformation and improve the structure's ductility index by limiting stress transmission to other components.

3.3 Load-strain curves

Figs. 8(a~d), **9(a~h)**, and **10(a~h)** depict load-strain curves and magnitudes on UCs and LCs, highlighting the strain amount, yield strain, and local buckling sites, while **Fig. 11(a~c)** shows the part-wise maximum absolute strain distribution on corner fittings, UCs, LCs, FBs, and CBs. The curves exhibit linear, nonlinear, and recession sections. As load increases, stress rises until local buckling is indicated by inversion, overturning, or abrupt decline in strain curves with exceptionally high values. Curves overturning before or near yield strain signify stresses below the yield strength, causing elastic buckling. Conversely, plastic buckling occurs with stresses surpassing yield. Post-yield overturning curves during the recession phase indicate severe local plastic buckling. Inward and outward buckling occurs in the upper column's lower region, while other members lack buckling or yielding, as indicated by lower strain values in upper and lower corner fittings, highlighting the absence of localized deformation in rotary IMCs. For instance, locations 2, 19, 20, 30, 43, and 44 in RS1, locations 2, 3, 24, 36, 50, 51, and 52 in RS2, and locations 2, 3, 4, 23, 24, 25, 34, 35, 46, and 47 in RS3 demonstrate the existence of local buckling on each face of UCs lower regions, which exhibits elastic and plastic local buckling. Portions of UCs experiencing bending stresses in or opposite directions of beams display elastic buckling. In contrast, adjacent sides of UCs not exposed to bending undergo plastic buckling. For instance, 19, 20, 43, and 44 in RS1, 50, 51, and 52 in RS2, and 23, 24, and 25 in RS3 display local elastic buckling, suggesting that bending and the *P*-Delta effect prevent UCs and other

members from yielding fully. This reveals that the CMSFs' instability is mainly driven by geometric instability, as opposed to IMCs or members' strength failure.

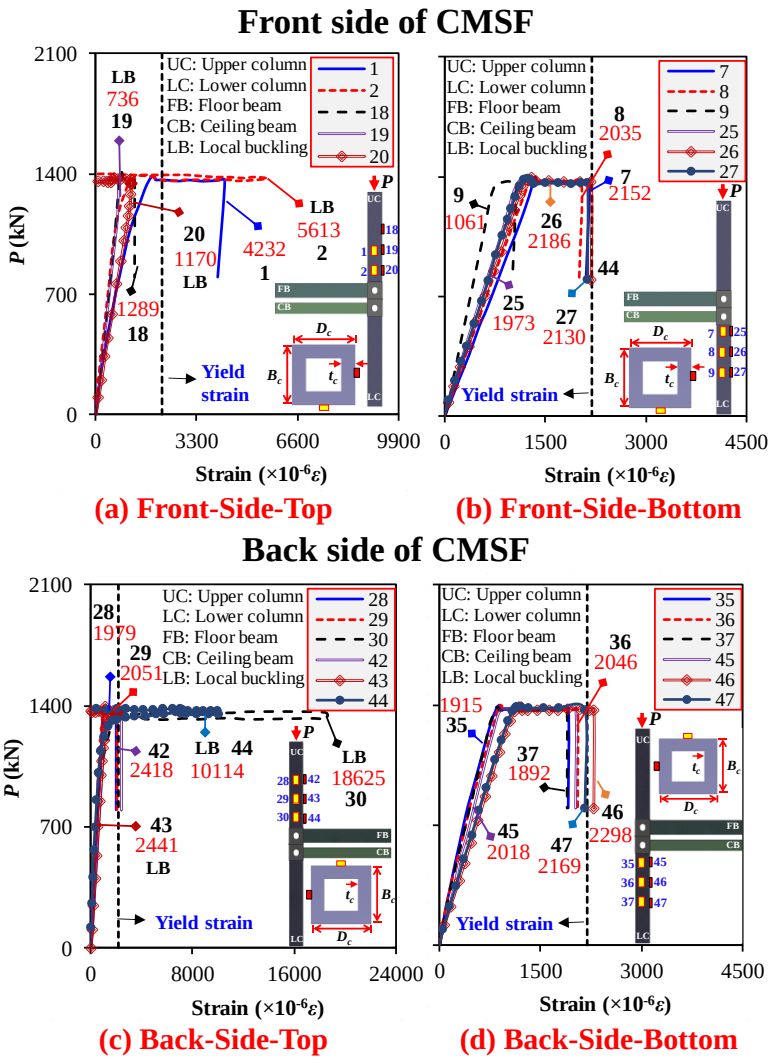

Fig. 8 Load-strain curves at columns of RS1

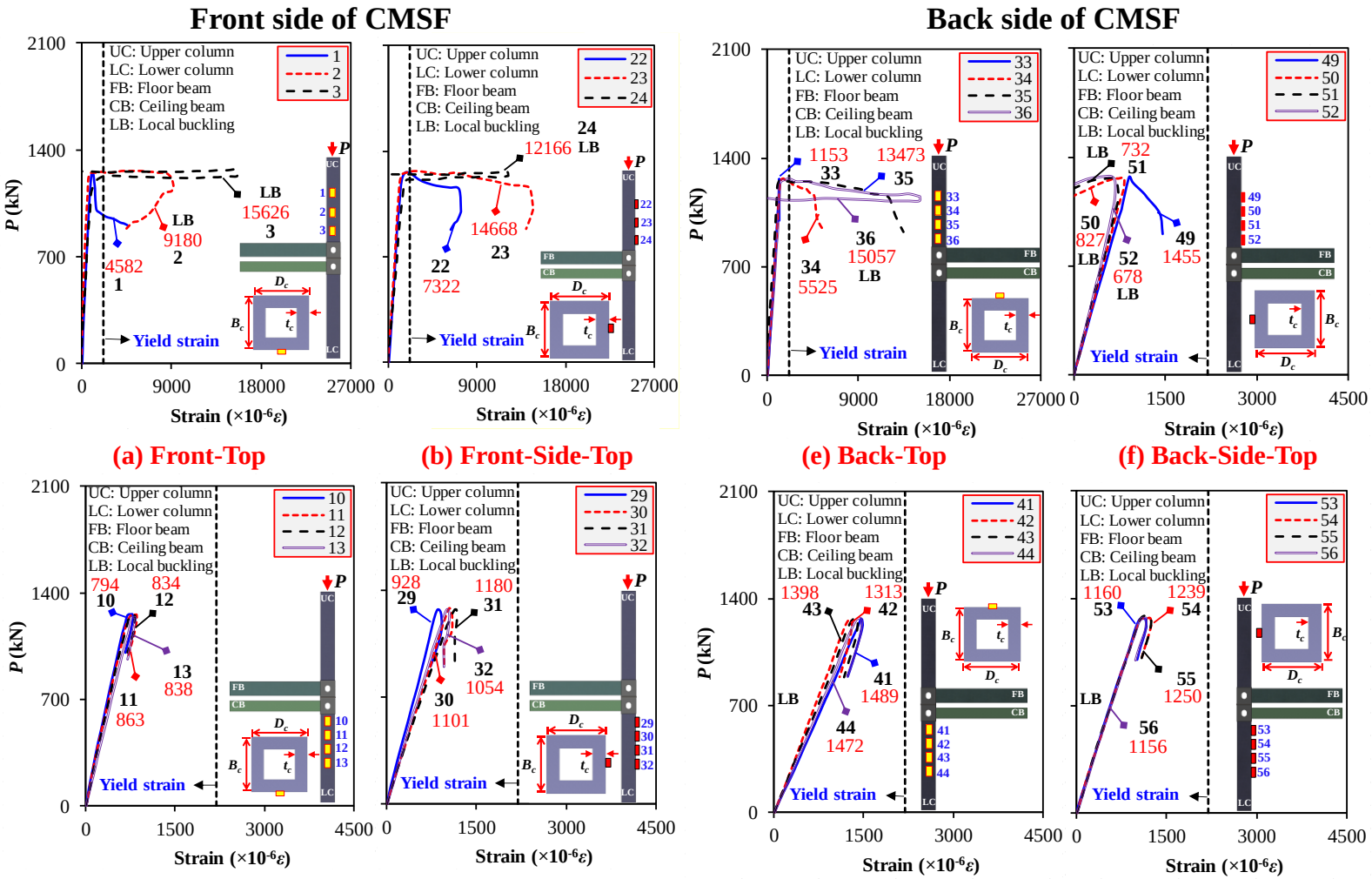

Fig. 9 Load-strain curves at columns of RS2

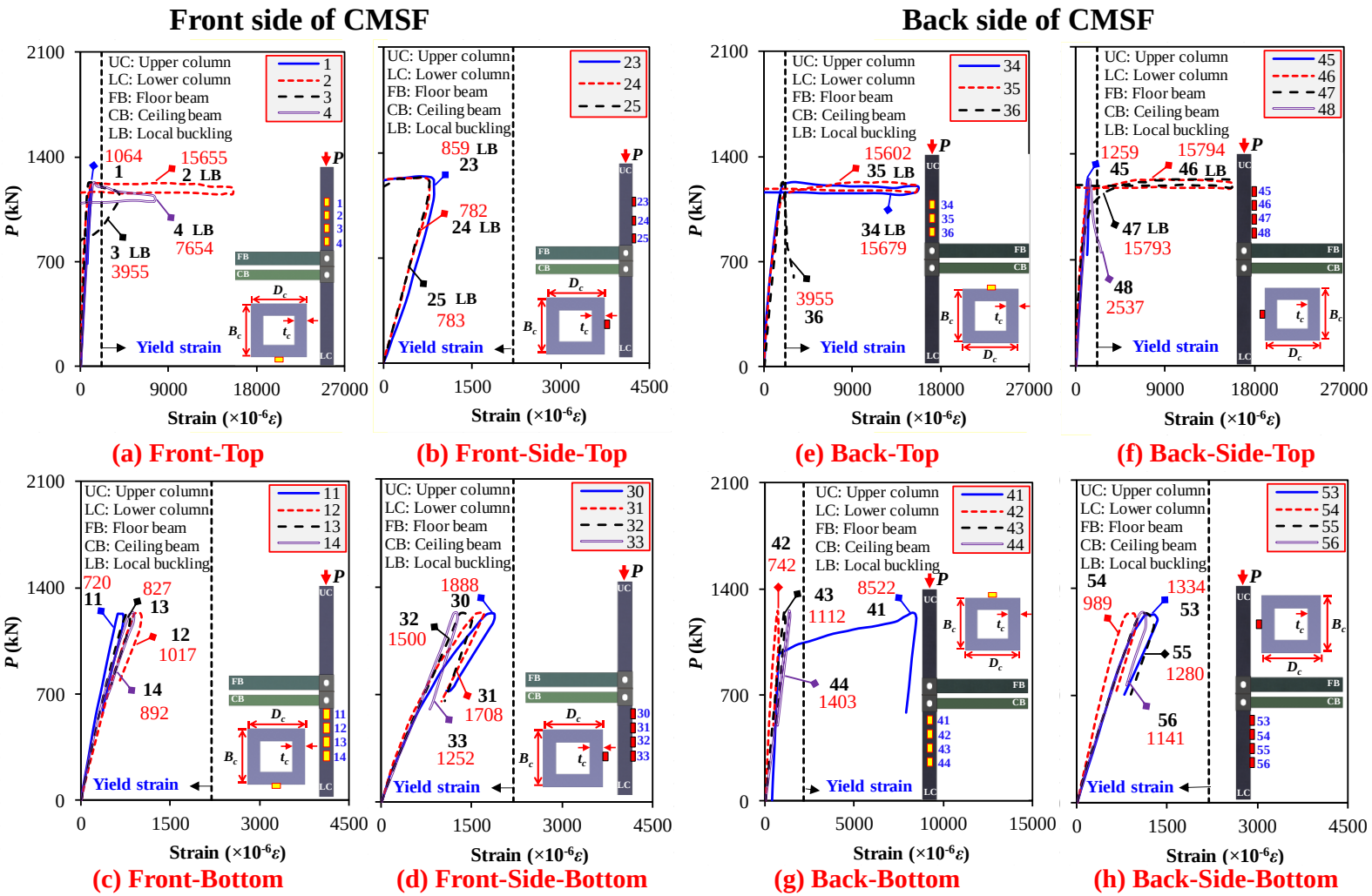

Fig. 10 Load-strain curves at columns of RS3

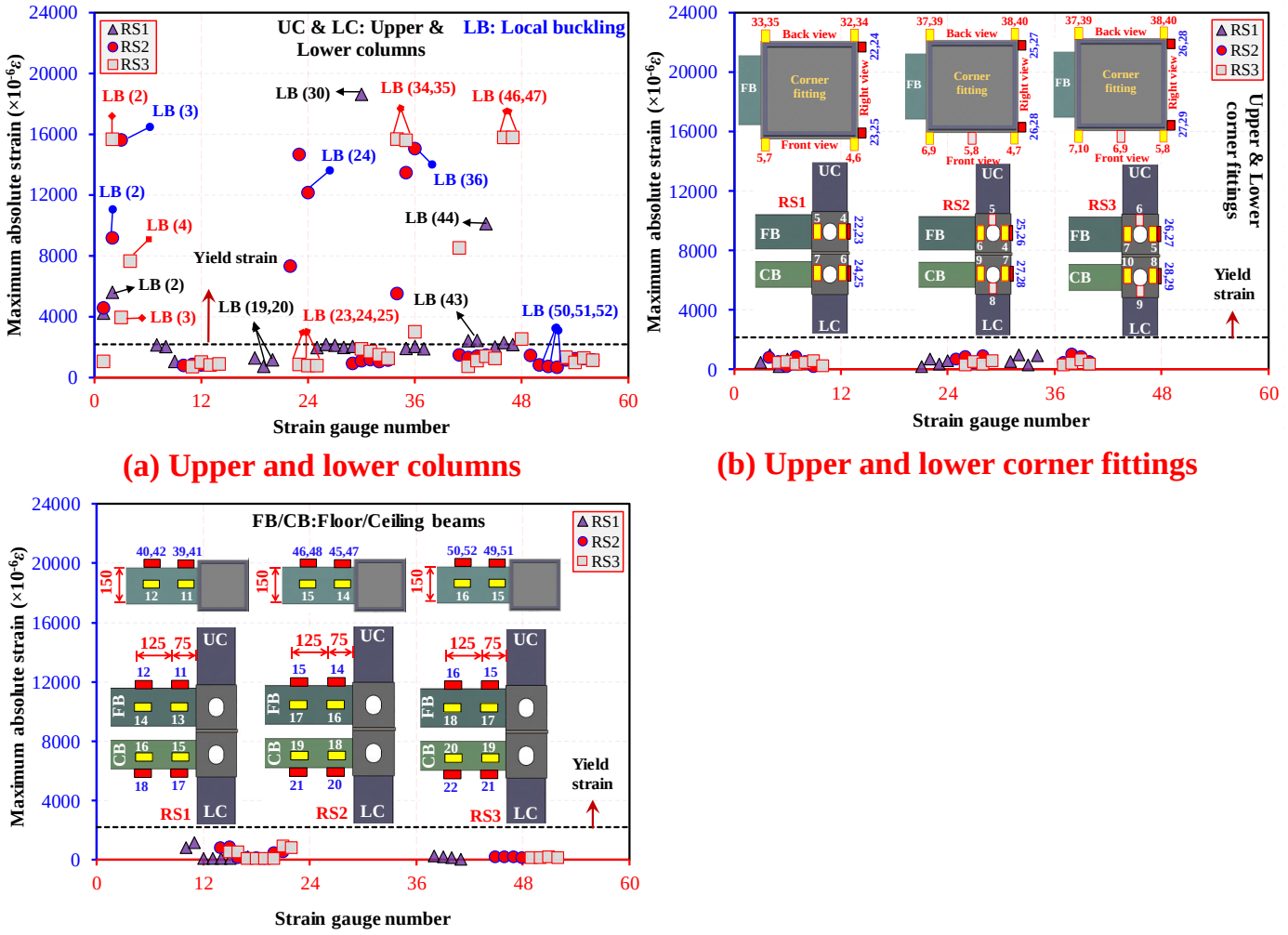

Fig. 11 Part-wise maximum absolute strain distribution

3.4 Load-deflection curves

Fig. 12(a~f) shows the load-deflection curves where the compressive load is denoted by P, and δ signifies the lateral deflection of the columns and the vertical and lateral deflections of the beams. They operate with linear and nonlinear stages, with a lengthy recession phase followed by a curve drop. This is because the failure of CMSFs is limited to bending and local buckling of UCs with sway. While the load increases, the deflection also rises, stabilizing when the ultimate capacity is reached, followed by a pause in load but deflection increments. The orderly increase in lateral deflection from LCs to UCs indicates the presence of CMSF sway, denoted by Δ_c. Simultaneously, the maximum deflection at the top of the UCs suggests CMSFs' instability due to local and global failure. Alternatively, non-identical deflections of FBs and CBs in vertical and lateral directions and their difference imply a degree of relative rotation between the upper and lower frame skeleton at IMCs, which cannot be simulated as rigid or pinned [30]. The varied stiffness decrement of each curve reveals that members act differently with the secondary moment amount they experience. RS3 exhibited a more notable nonlinear stage followed by more significant deflection than RS1 and RS2, indicating that less rigid beams translate more, enhancing CMSF flexibility and force distribution among members. The deflection curve supports test failure modes. Notably, the deflection difference between UC ends (H8 and H6) suggests local buckling initiation near H6, followed by increased top lateral deflection.

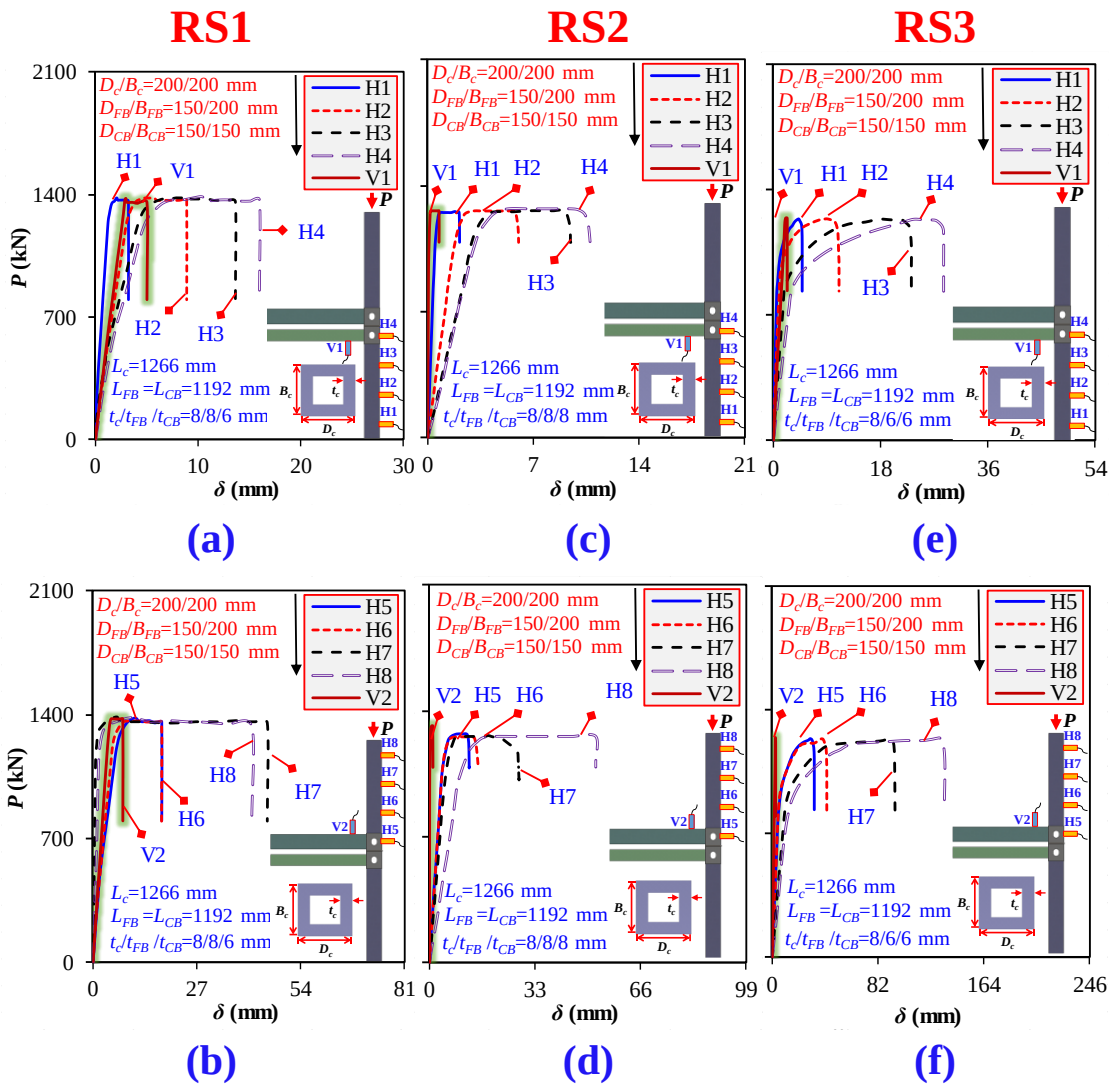

Fig. 12 Load-deflection curves at various parts of tested CMSFs

4 Finite element analysis on CMSFs with rotary IMCs

The test yielded valuable data but did not assess CMSF's overall instability and the influence of altering parameters. To create a reliable FEM, test failure modes and data from load-shortening curves were used.

4.1 Formation of finite element model

The finite element modeling and analysis were conducted with ABAQUS [135]. Elastic buckling was performed using the ABAQUS/Linear perturbation buckle-type solver and the subspace iteration approach to determine the buckling loads and modes. Then the nonlinear analysis adopted the ABAQUS/static Riks-type solver to determine the load-shortening and failure mechanism. Moreover, the bilinear kinematic hardening

and the von Mises yield criteria were adopted for all components utilizing the associated material properties listed in **Table 1** [30]. The Poisson's ratio of 0.3 was adopted [78].

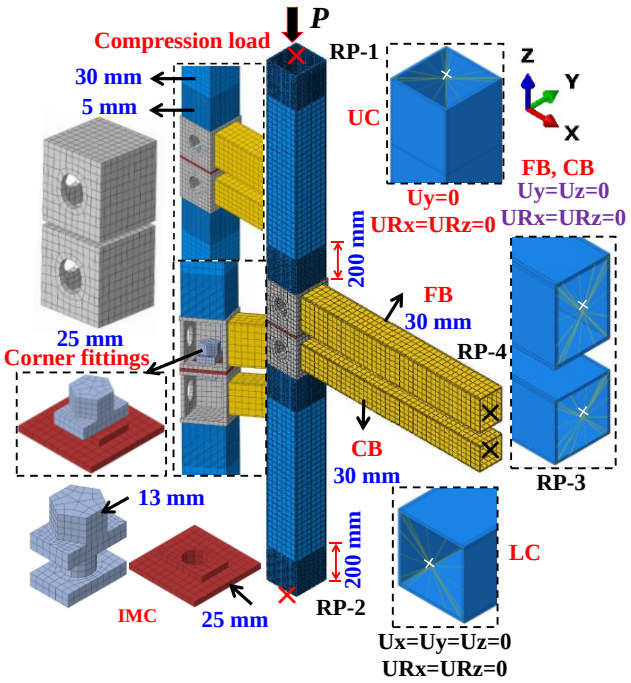

(a) Verified FEM details of CMSF with rotary IMC

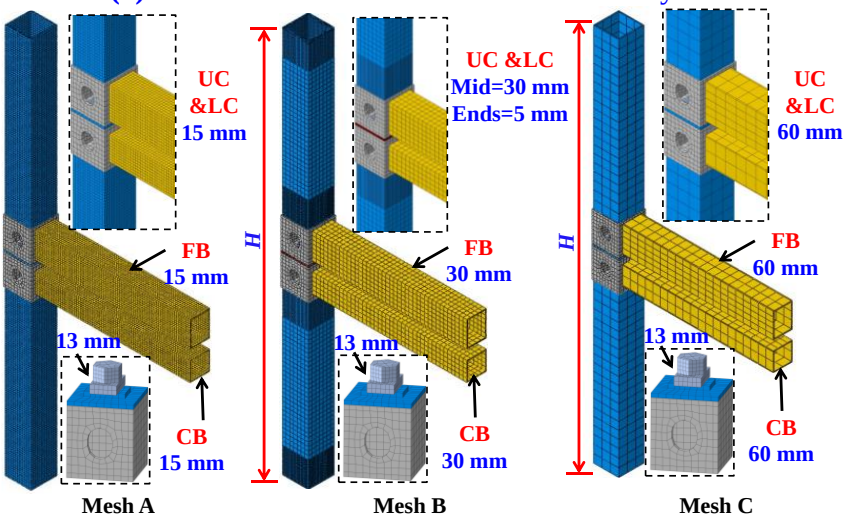

(b) Selected mesh details for FEM validation of CMSF

Fig. 13 Experimentally-verified FEM details of CMSFs with rotary IMCs

4.2 Mesh modeling

Fig. 13(a) illustrates the test-validated CMSFs mesh model. Members' dimensions matched the specimen's design, which was modeled using C3D8R elements [49]. The suitability of the element size was determined by a mesh convergence study that employed mesh A, B, and C and compared their results with test *P-Δ* curves, as depicted

in **Fig. 17(d)**. To accurately replicate local buckling, the column edges at 200 mm were densely meshed, whereas other parts were meshed uniformly. Additionally, the corners of columns and beams were partitioned at their thickness to create the structured mesh [68–71]. Types A and B assessed local buckling and deformation at the column ends more precisely than Type C, shown in supplementary **Fig. B1(h)**. When mesh was raised from 15 to 30 and 60 mm, P_u (K_e) increased by up to 32% (6%) while Δ_u and DI by 11%. Mesh sizes significantly impacted failure modes and compressive behavior, revealing that Type B with 30 mm mesh yielded the closest results. This highlighted the importance of compressive tests on CMSFs with rotary IMCs to determine the proper mesh density.

4.3 Loading and boundaries

Reference nodes (RP-1~RP-4) on column and beam cross-sections with surface-based coupling constraints that limit translation and rotation provided loading and boundary conditions. Vertical translations of beams were constrained, whereas those of LCs were restricted in all directions. While UCs and beams had the freedom of in-plane translation, the out-of-plane translation and rotation of beams and columns were restrained. Compression force was applied on the UC as displacement-controlled loading to achieve shortening. Columns and beams were welded to corner fittings using "tie constraint" via surface-to-surface contact. The interaction between corner fittings, connecting plates, and IMC components was simulated as surface-to-surface with "hard contact" as normal while "finite sliding" as tangential behavior [48]. A friction coefficient of 0.3 was chosen, as shown in **Figs. 17(e)** and supplementary **Fig. B1(i)** [49,65]. All specimens used hot-rolled sections with low bending, welding deformation, and residual stresses; thus, the effects of bending, welding, and temperature residual stress were omitted in FEMs [136,137].

4.4 Initial imperfections

The CMSFs' components might have imperfections before and after installation, which is difficult to measure by conventional methods [134]. Design standards prescribe imperfections between t_c/500 to t_c/200 and L_c/1000 to L_c/1996 [138]. However, for CMSFs, imperfections can be attributed to column thickness (t_c), frame height (H), and eccentricity (e) [47,91,92,139]. This study selected height imperfection values of H/500, H/1000, H/1500, and H/2000; thickness imperfection values of t_c/1000, t_c/100, t_c/10, t_c, and $2t_c$; and load eccentricities of 0, D_c/70, D_c/35, D_c/14, $4D_c$/14, $6D_c$/14, $3.35D_c$/7, and $3.43D_c$/7. Eigenvalue analysis yielded the buckling modes shown in **Fig. 15(a~c)**. In addition to thickness or height imperfections, nonlinear Riks analysis applied load eccentricities per test failure mode depicted in **Fig. 7(a~c)**, such as in the direction of beams for RS1 and RS3 and the opposite direction of beams for RS2. A comparison was made between the critical buckling loads and accompanying mode shapes and the loads at which failure occurred in the Riks analysis. Incorporating global stability parameters offered insights into individual buckling modes' contribution and highlighted local buckling's role in overall stability, improving CMSFs' stability assessment and understanding of buckling modes' interaction. The load corresponding to the first buckling mode was 1312.5 kN for RS1, which exhibited a compressive resistance of 1397 kN. To assure a reliable description of the structure's behavior, imperfections were introduced to the lowest buckling mode (Mode 1) for RS1, RS2, and RS3 [77]. The imperfection amplitude determined in **Fig. 14(a~c)** was utilized for all CMSFs and FEMs in Supplementary **Table A1**. Compared with test results, local imperfection of H/600 or $0.64t_c$ and global imperfection of e=$3.35D_c$/7 yielded the closest results. The influence of increasing H or t_c imperfection values on P_u (K_e) and Δ_u (DI) was non-apparent. Since in CMSFs, translation or rotation was allowed; thus

the eccentricity impact was significant, as depicted in failure modes in supplementary **Fig. B1(j)**.

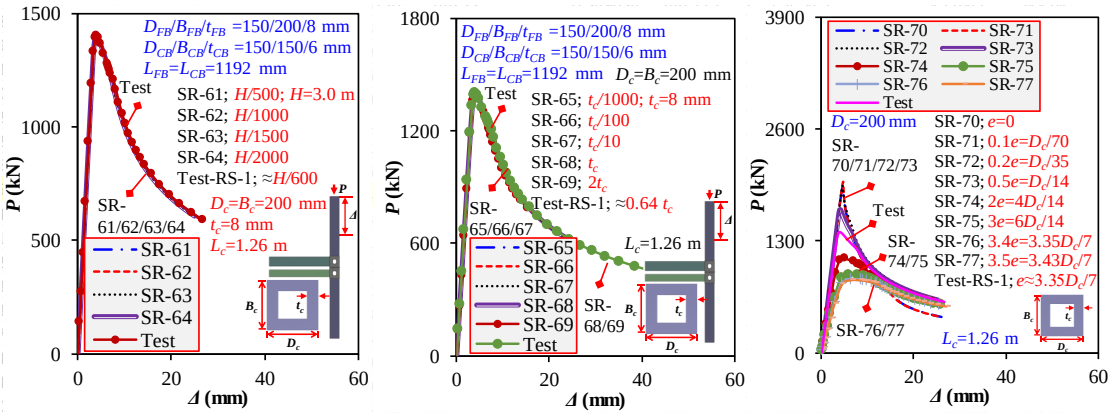

(a) Local imperfection *H* **(b) Local imperfection t_c** **(c) Global imperfection *e***

Fig. 14 Influence of initial imperfections

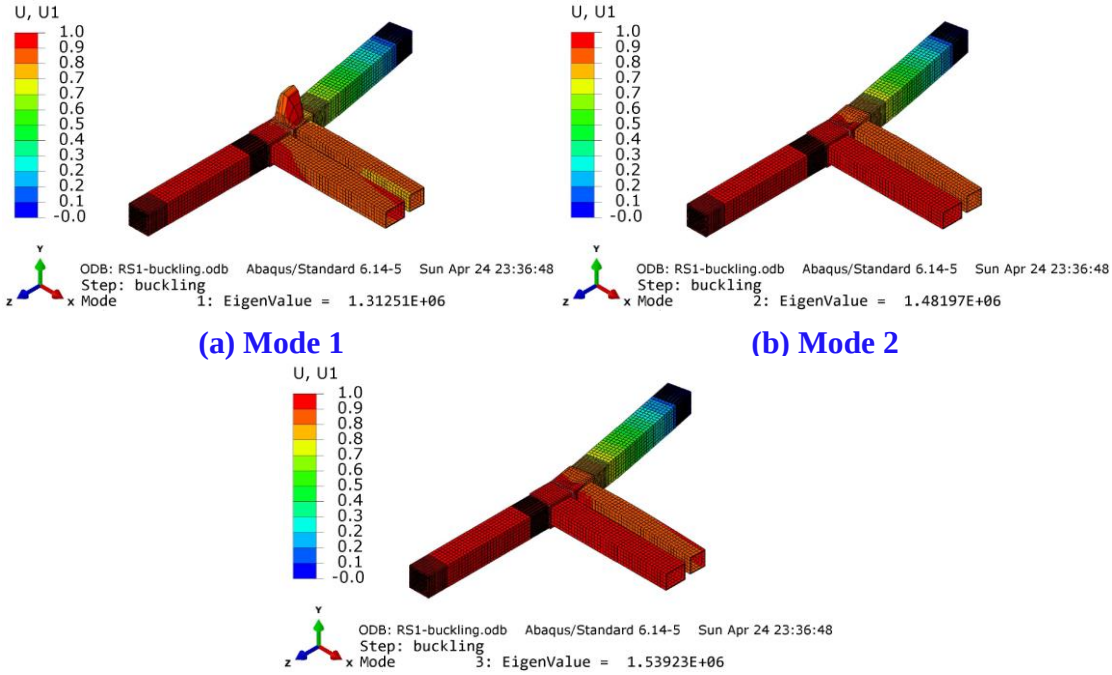

(a) Mode 1 **(b) Mode 2**

(c) Mode 3

Fig. 15 First three buckling modes

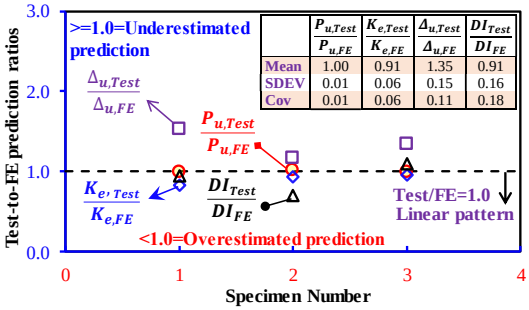

Fig. 16 Comparisons of Tests-to-FEM of CMSFs

4.5 Validations

The average estimates for P_u, K_e, Δ_u, and DI made by the FEMs for three tests on RS1, RS2, and RS3 are shown in **Figs. 16** and **17(a~c),** and **Table 1**. The FEMs produced average modest prediction errors of 0.3%, 9.1%, and 8.5% for P_u, K_e, and DI but exhibited a significant scattering of 35% for Δ_u, principally brought on by FEM simplifications, soft supports, material modeling, and variations in imperfection. The developed FEM can adequately simulate CMSFs' deformed shapes with inward and outward LB at the UCs' lower area and sway, as depicted in **Fig. 18(a~c)**, validating the FEMs' reliability to anticipate the CMSFs' compressive behaviors with rotary IMCs.

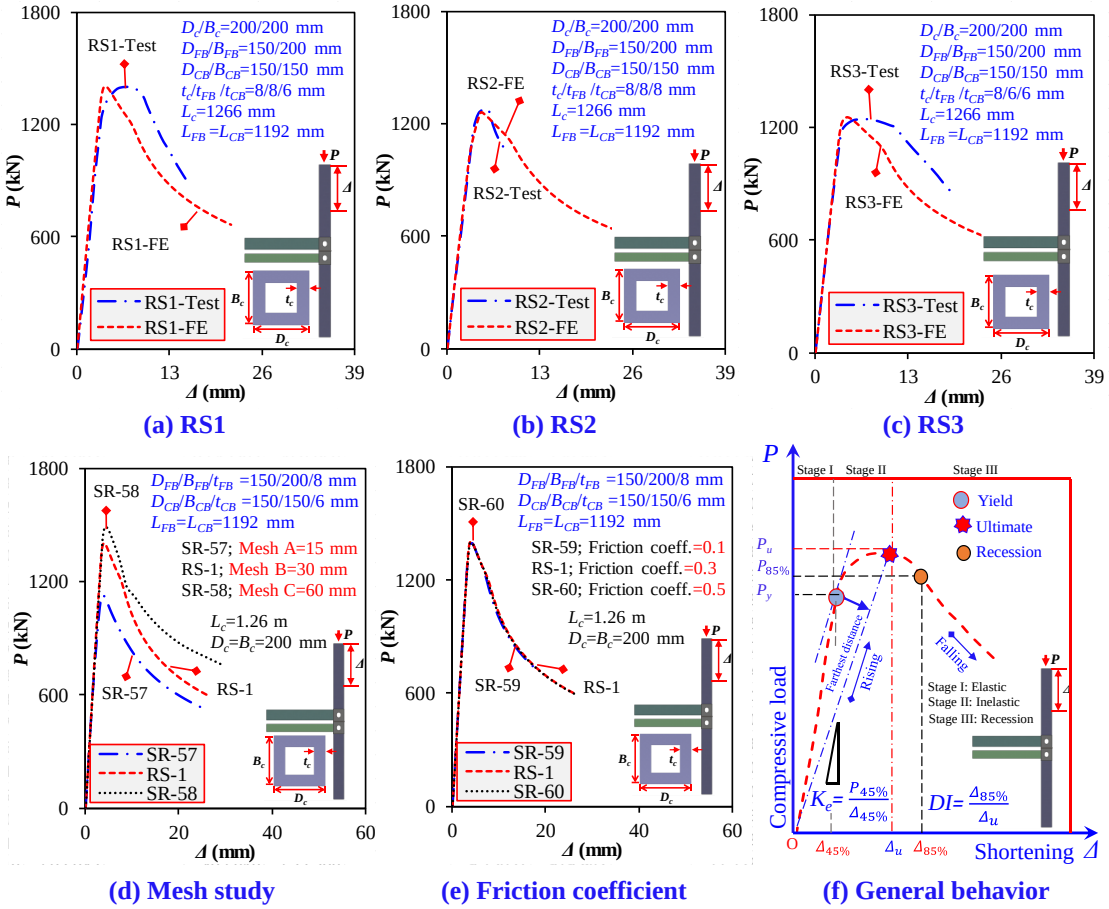

(a) RS1 (b) RS2 (c) RS3

(d) Mesh study (e) Friction coefficient (f) General behavior

Fig. 17 Load-shortening curves of CMSFs

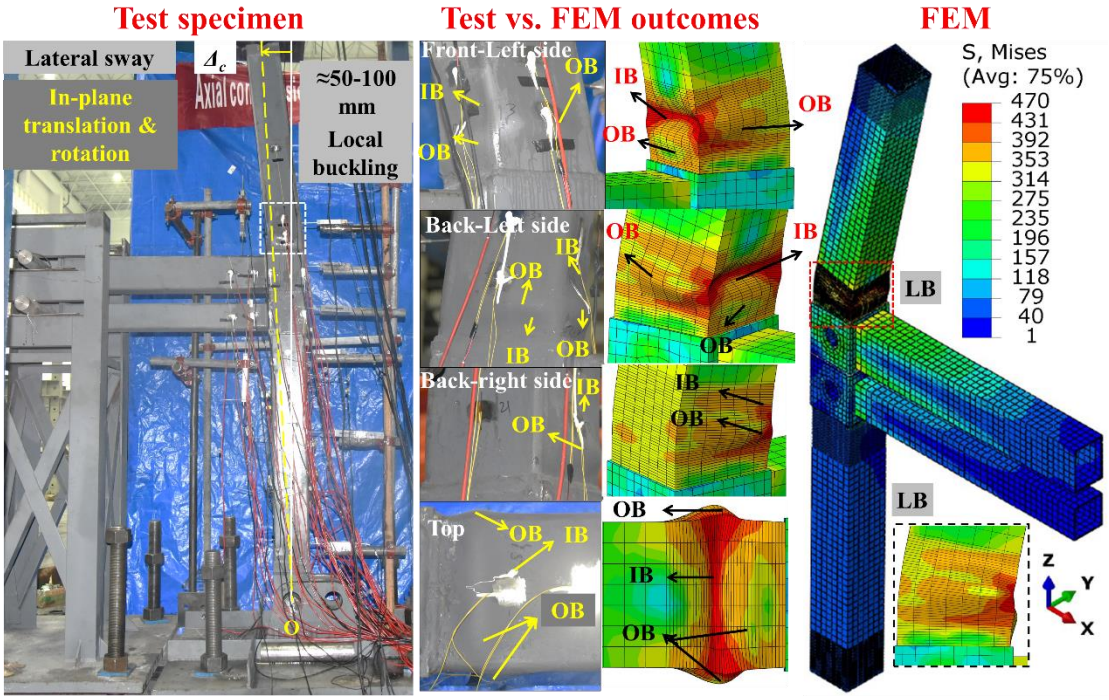

(a) RS1 specimen

473

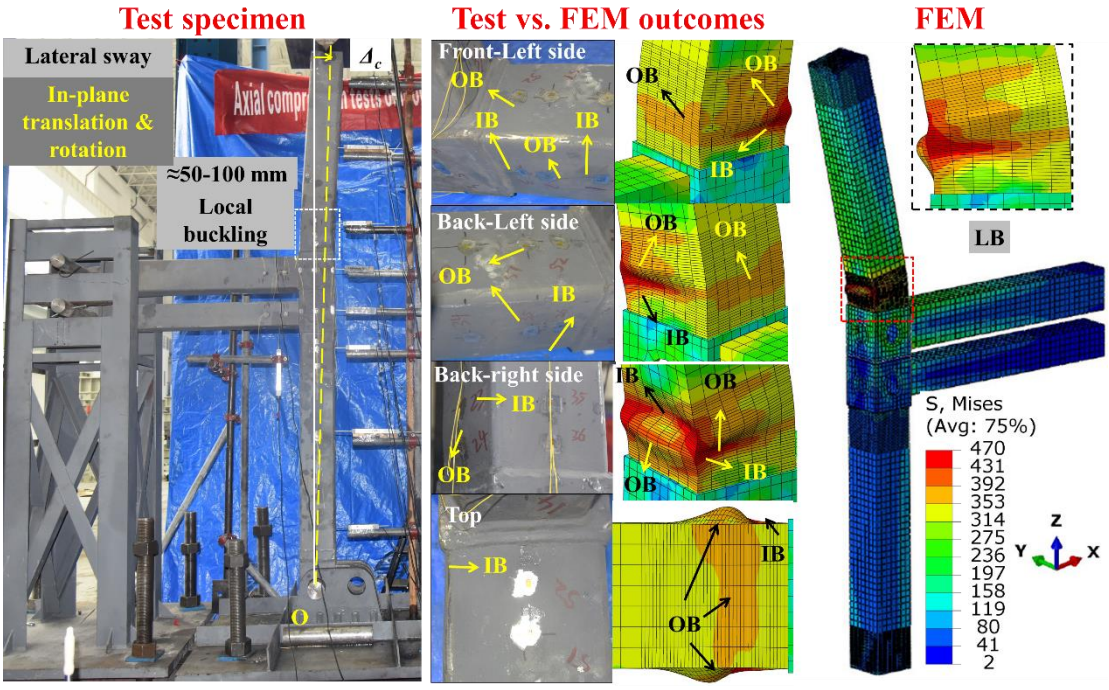

(b) RS2 specimen

474

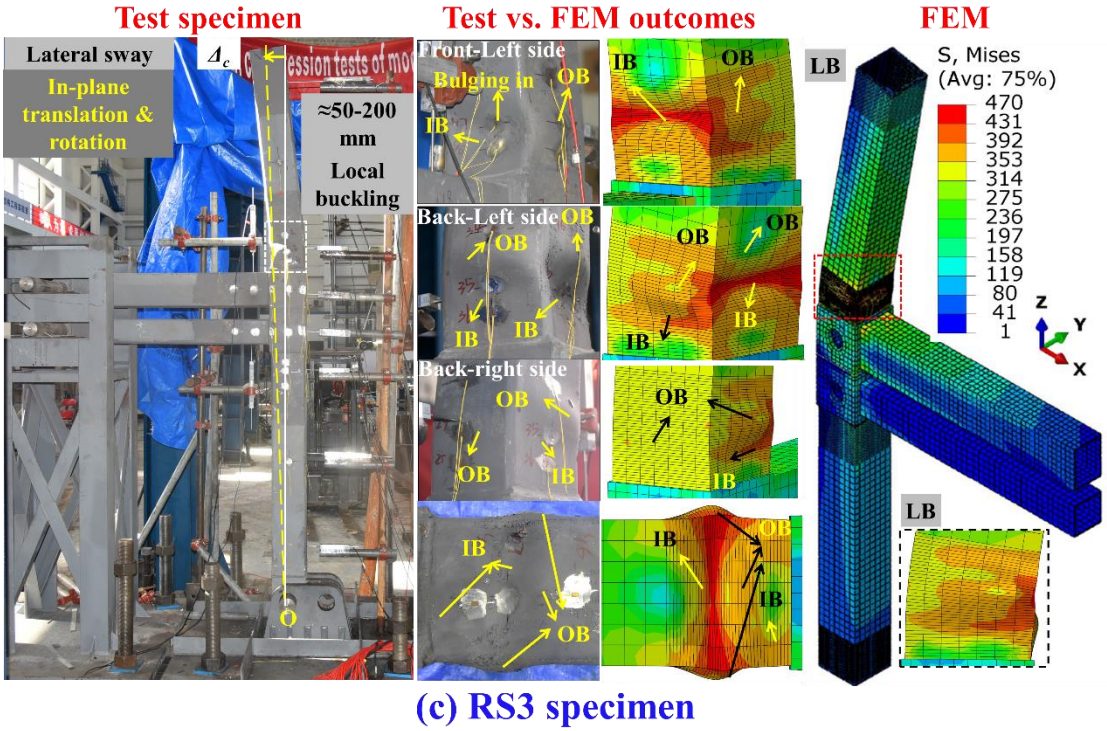

Fig. 18 Test vs. FE-predicted failure modes

5 Parametric analysis

Data for 77 CMSFs was produced using validated FEM that maintained the rotary IMC and corner fittings dimensions, mesh B, local imperfection of $H/600$ or $0.64t_c$, and global imperfection of $e=3.35D_c/7$. The parametric analysis covered beam and column sizes, lengths, spacing, and plate thicknesses. Typical load-shortening and failure behaviors were classified in **Figs. 19(a~g)** and **20(a~f)**, showing similar patterns to the test results. Supplementary **Figs. B1(a~j), B2(a~g),** and **B3(a~g),** along with **Table A1**, offered detailed information about the specific parameters and their comprehensive impact on failure modes, P_u-K_e trends, Δ_u-DI trends, and the values of P_u, K_e, Δ_u, and DI.

5.1 Beams sizes (D_{FB}×B_{FB}×t_{FB}; D_{CB}×B_{CB}×t_{CB})

Fig. 19(a) demonstrates how the compressive behavior of CMSFs is influenced by variations in floor and ceiling beam sizes, such as D_{FB}, D_{CB}, B_{FB}, B_{CB}, t_{FB}, and t_{CB}, ranging from 150 to 200 mm and 6 to 8 mm while maintaining their lengths. Increasing the beam sizes has a positive impact on the CMSFs' performance, enhancing P_u, K_e, Δ_u,

and *DI*, with improving P_u (K_e) by up to 46% (10%) and Δ_u (*DI*) by 15% (19%). This improves frames' compressive behavior and bending resistance. It can prevent premature buckling and improve ductility, allowing CMSFs to deform more before reaching capacity, as shown in Supplementary **Fig. B1(a)**.

5.2 Beams lengths (L_{FB}; L_{CB})

The compressive behavior of CMSFs can be influenced by floor and ceiling beam length variations, as shown in **Fig. 19(b)**. The results indicate that increasing the beam lengths from 0.6 to 1.2 and 3 m for a given D_{FB}, D_{CB}, B_{FB}, and B_{CB} of 150 and 200 mm and t_{FB} and t_{CB} of 8 and 6 mm could harm the compressive performance of the CMSFs by impairing P_u (K_e) up to 37% (5%). The increased slenderness of longer beams reduces bending resistance and may cause premature buckling, preventing CMSFs from achieving full capacity. Supplementary **Fig. B1(b)** demonstrates that it might improve ductility by enhancing column-beam flexibility when adequately built**.**

5.3 Columns lengths (L_c)

The compression behavior of CMSFs can be affected by changes in the length of the columns, as depicted in **Fig. 19(c)**. The findings demonstrate that elongating the columns from 0.6 to 1.2 and 3 m for a given L_{FB} and L_{CB} of 0.6, 1.2, and 3 m, D_{FB}, D_{CB}, B_{FB}, and B_{CB} of 150 and 200 mm, and t_{FB} and t_{CB} of 8 and 6 mm may harm the CMSFs' performance by decreasing their P_u (K_e) by up to 65% (71%). This occurs because longer columns become more slender, reducing their resistance to buckling and bending, which can increase deflection and bending stresses, limiting CMSFs' load-carrying capacity. However, redistribution of forces within the frame might improve the ductility, as demonstrated in Supplementary **Fig. B1(c)**.

5.4 Columns sizes (D_c×B_c)

Changes in the size of the columns can impact the behavior of CMSFs when subjected to compression, as shown in **Fig. 19(d)**. The results indicate that enhancing the cross-

sectional sizes from 150 to 180, 200, and 210 mm for a given L_c, L_{FB}, and L_{CB} of 1.2, 2.5, and 3.6 m and t_c of 8 mm can improve the performance of CMSFs by increasing their P_u (K_e) up to 140% (116%) but may also have adverse effects by reducing Δ_u (DI) up to 41% (10%). Increasing D_c and B_c improves column buckling and bending resistance and decreases slenderness. As illustrated in Supplementary **Fig. B1(d)**, increasing D_c/t_c yields a wider cross-section, reducing CMSF buckling strain and ductility.

5.5 Columns thickness (t_c)

In **Fig. 19(e)**, column thickness affects CMSF compression behavior. The results show that increasing column cross-section thickness from 6 to 8 and 10 mm for D_c and B_c of 150, 180, 200, and 210 mm can improve CMSF performance by raising their P_u (K_e) by up to 123% (55%) and Δ_u (DI) by up to 16% (113%). A decrease in D_c/t_c reduces column slenderness and increases buckling and bending resistance. Thus, CMSFs can withstand more plastic deformation before failure, increasing their buckling strain and ductility, as depicted in Supplementary **Fig. B1(e).**

5.6 Beams gap and connecting plate thickness

Figs. 19(f, g) and **B1(f, g)** demonstrate that CMSF compressive behavior remained unaffected by increasing the beam gap from 20 to 74 and 133 mm and the connecting plate thickness from 5 to 15 and 30 mm. These factors can affect the frame's lateral rigidity, yet CMSF columns resist compressive stresses, indicating that rotary IMC can transmit compressive loads without localized failure to CMSFs, as depicted in Supplementary **Figs. B1(f)** and **B1(g)** [14,47].

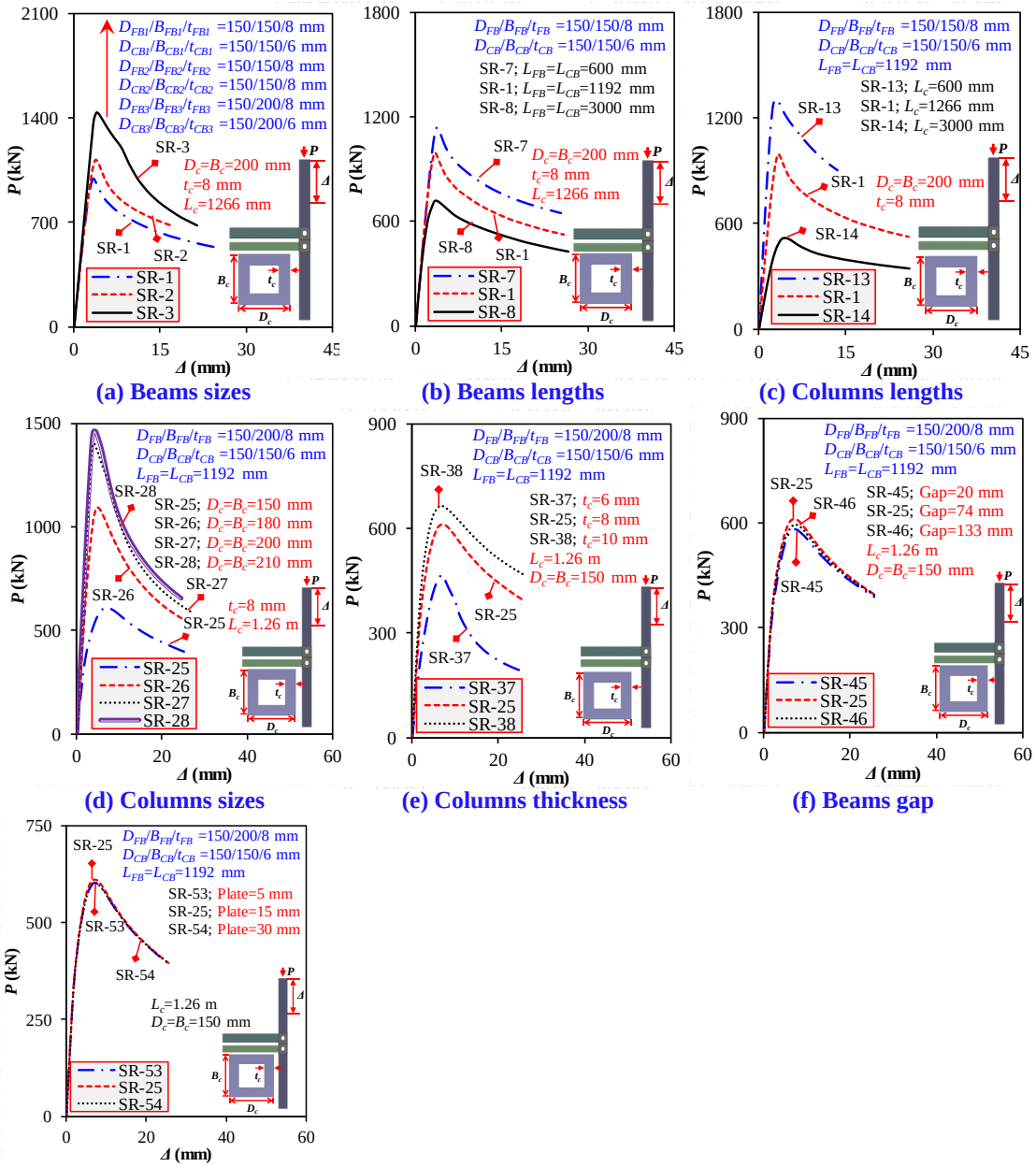

Fig. 19 Influence of varying parameters on CMSFs' load-shortening curves

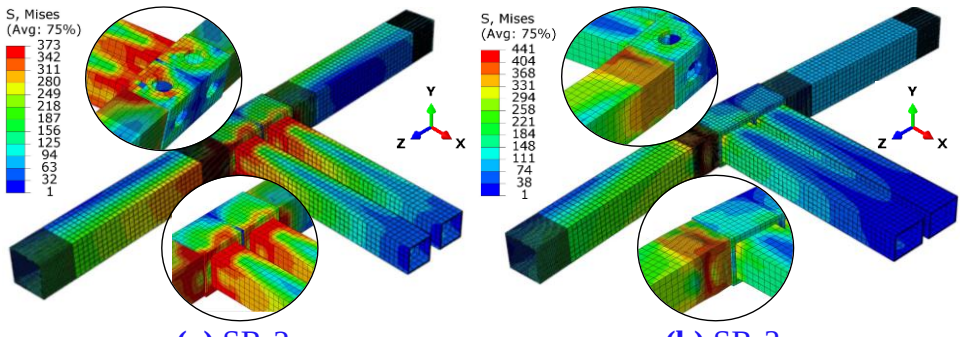

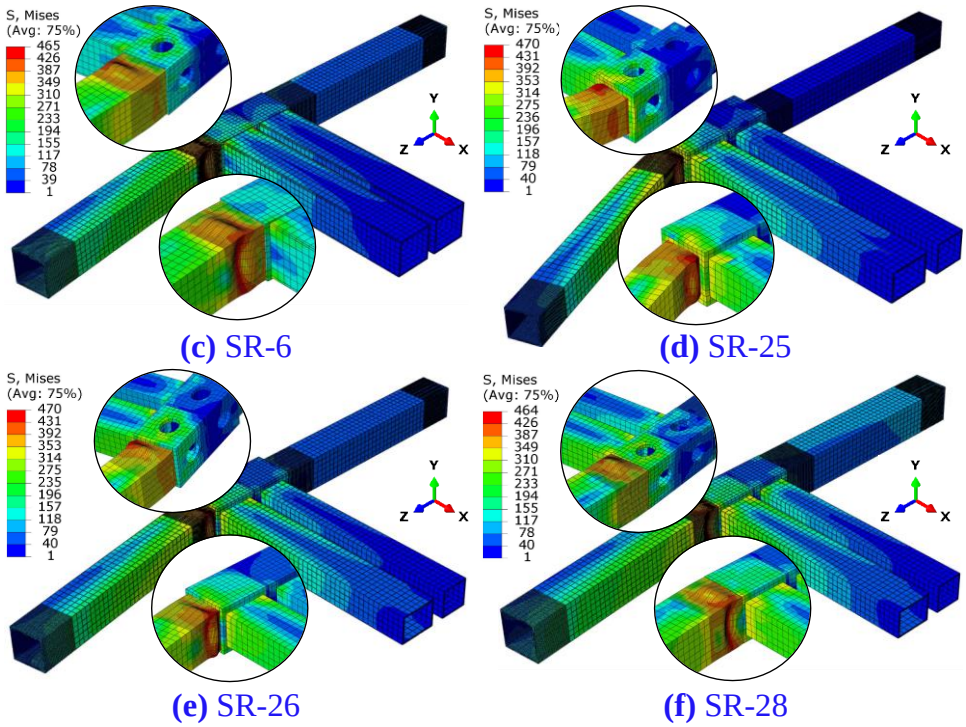

Fig. 20 CMSFs' typical failure modes against compressive loading

6 Theoretical investigations on CMSFs with rotary IMCs

The failure mechanism observed in CMSFs reveals both elastic and plastic local inward and outward buckling in the upper columns. This observation indicates noncompliance with EC3 Class 3 slenderness criteria, as elastic buckling is restricted, prohibiting complete cross-section yielding. Local buckling has a significant impact on member capacities, whether it is plastic or elastic [140]. Incorporating global strength while accounting for global stability parameters yields more conservative results than cross-sectional strength assessments under these conditions [86]. Multiple studies demonstrate consistent design practices in which global strength prediction is utilized for member design, considering yield strength failure due to local buckling of Class 3 columns [141,142]. Certain investigations include local buckling reduction factors for fixed-ended stubs [143], while others prefer member buckling strength as the primary design criterion [144]. Likewise, global buckling strength models are applied to simple-supported, concentrically compressed members [140]. Notably, IS800 [145,146], NZS 3404[147], EC3:1-1 [148], CSA S16-19 [149], AISC360-16 [150], and GB 50017-2017

[115] highlight the vitality of effective length factors in stability design, depending on the degree of elastic restraint at frame column ends. The unique characteristics of MSB discontinuous columns and IMCs introduce variability in their effective length factor and buckling load, governed by the relative joint and member bending stiffness ratio and the stiffness of IMCs [81]. Chen et al. [151] underscore that insufficient IMC stiffness can amplify MSB column slenderness, necessitating stability analysis for a conservative determination of critical buckling load. Thus, while assessing CMSF compressive behavior, the critical buckling load that causes the frame to buckle is the main focus. Buckling load equations for the tested sub-assembled CMSFs in **Fig. 21(a)** are determined. The derivation uses pinned and semi-rigid IMCs in three-story full-scale models shown in **Fig. 21(b)**. The stability functions presented in Eqns. 1 and 2 [152], along with the buckling load equation in Eqn. 3 [106] are utilized.

$$S_{ii} = \frac{\left(\frac{\pi}{\mu}\right)^2 - \frac{\pi}{\mu}\sin\frac{\pi}{\mu}}{2 - 2\cos\frac{\pi}{\mu} - \frac{\pi}{\mu}\sin\frac{\pi}{\mu}}\ ;\ S_{ij} = \frac{\frac{\pi}{\mu}\sin\frac{\pi}{\mu} - \left(\frac{\pi}{\mu}\right)^2\cos\frac{\pi}{\mu}}{2 - 2\cos\frac{\pi}{\mu} - \frac{\pi}{\mu}\sin\frac{\pi}{\mu}} \quad \text{for } c_1, c_2, \text{and } c_3 \tag{1}$$

$$S_{ii} = 4\ ;\ S_{ij} = 2 \quad \text{for } b_1, b_2, b_3, \text{and } b_4 \tag{2}$$

$$P_{cr} = \left[\pi^2 EI_{c2} \Big/ (2\mu L_{ct})^2\right] \tag{3}$$

6.1 Pinned IMCs

Following Chen et al.'s model [106], using the target column c_2 shown in **Fig. 21(c)**, the members' moments and their equilibrium at joints A, B, and sway are determined from Eqns. 4~8 as follows;

$$(M_A)_{c2} = \left(EI_{c2}/L_{c2}\right)\left[S_{ii}\theta_A + S_{ij}\theta_B - \left(S_{ii} + S_{ij}\right)\Delta_c/L_{ct}\right] \tag{4}$$

$$(M_B)_{c2} = \left(EI_{c2}/L_{c2}\right)\left[S_{ij}\theta_A + S_{ii}\theta_B - \left(S_{ii} + S_{ij}\right)\Delta_c/L_{ct}\right] \tag{5}$$

$$(M_A)_{b2} = \left(EI_{b2}/L_{b2}\right)[4\theta_A + 2\theta_B] = \left(EI_{b2}/L_{b2}\right)[6\theta_A] \tag{6}$$

$$(M_B)_{b3} = \left(EI_{b3}/L_{b3}\right)[4\theta_B + 2\theta_A] = \left(EI_{b3}/L_{b3}\right)[6\theta_B] \tag{7}$$

$$(M_A)_{c2} + (M_A)_{b2} = 0; (M_B)_{c2} + (M_B)_{b3} = 0;\ (M_A)_{c2} + (M_B)_{c2} + P\Delta_c = 0 \tag{8}$$

$$\theta_A(S_{ii} + 6G_C) + \theta_B(S_{ij}) + \Delta_c/L_{ct}\left[-\left(S_{ii} + S_{ij}\right)\right] = 0\ ;\ G_C = \frac{EI_{b2}/L_{b2}}{EI_{c2}/L_{ct}} \tag{9}$$

$$\theta_A(S_{ij}) + \theta_B(S_{ii} + 6G_D) + \Delta_c/L_{ct}\left[-\left(S_{ii} + S_{ij}\right)\right] = 0;\ G_D = \frac{EI_{b3}/L_{b3}}{EI_{c2}/L_{ct}} \tag{10}$$

$$\theta_A(S_{ii}+S_{ij})+\theta_B(S_{ii}+S_{ij})\ -{}^{\Delta_c}/_{L_{ct}}\left[2(S_{ii}+S_{ij})-\left({}^{\pi^2}/_{\mu^2}\right)\right]=0 \tag{11}$$

where $P=\frac{\pi^2 EI_{c2}}{\mu^2 {L_{c2}}^2}$. After solving Eqns. 9~11 using determinant**,** Eqn. 12 is obtained to calculate the buckling length (μ), which is then inserted in Eqn. 3 to obtain buckling load (P_{cr}/PD) of a sub-assembled CMSF with rotary IMC, assuming as a pinned IMC.

$$\begin{aligned}(S_{ii}+6G_C)\left[\left\{\left({}^{\pi^2}/_{\mu^2}\right)-2(S_{ii}+S_{ij})\right\}\times\{S_{ii}+6G_D\}+(S_{ii}+S_{ij})^2\right]\\ -(S_{ij})\left[\{S_{ij}\}\times\left\{\left({}^{\pi^2}/_{\mu^2}\right)-2(S_{ii}+S_{ij})\right\}+(S_{ii}+S_{ij})^2\right]\\ -(S_{ii}+S_{ij})\left[(S_{ij})\times(S_{ii}+S_{ij})\ -(S_{ii}+S_{ij})\ \times(S_{ii}+6G_D)\right]=0\end{aligned} \tag{12}$$

6.2 Semi-rigid IMCs

According to Li et al.'s model [99], CMSFs in **Fig. 21(d)** bend in double curvature, so beams' end rotations are equal, such as $\theta_B=\theta_G;\ \theta_C=\theta_H;\ \theta_D=\theta_I;\ \theta_E=\theta_J$. Moreover, column end rotations are $\theta_A=\theta_C-\frac{M_B}{R_{1v}}\times\frac{\theta_D}{\theta_C},\ \theta_B=\theta_G=\theta_C-\frac{M_B}{R_{1v}},\ \theta_E=\theta_J=\theta_D-\frac{M_E}{R_{2v}}$, and $\theta_F=\theta_D-\frac{M_E}{R_{2v}}\times\frac{\theta_C}{\theta_D}$. Using slope-deflection equations, the moments of the members are obtained with Eqns. 13~20 as follows;

$$(M_{BA})_{c1}={}^{EI_{c1}}/_{L_{ct}}\left[S_{ii}\left(\theta_C-\frac{M_B}{R_{1v}}\right)+S_{ij}\left(\theta_D-\frac{M_B}{R_{1v}}\times\frac{\theta_D}{\theta_C}\right)-(S_{ii}+S_{ij})\,{}^{\Delta_c}/_{L_{ct}}\right] \tag{13}$$

$$(M_{CD})_{c2}={}^{EI_{c2}}/_{L_{ct}}\left[S_{ii}\theta_C+S_{ij}\theta_D-(S_{ii}+S_{ij})\,{}^{\Delta_c}/_{L_{ct}}\right] \tag{14}$$

$$(M_{DC})_{c2}={}^{EI_{c2}}/_{L_{ct}}\left[S_{ii}\theta_D+S_{ij}\theta_C-(S_{ii}+S_{ij})\,{}^{\Delta_c}/_{L_{ct}}\right] \tag{15}$$

$$(M_{EF})_{c3}={}^{EI_{c3}}/_{L_{ct}}\left[S_{ii}\left(\theta_D-\frac{M_E}{R_{2v}}\right)+S_{ij}\left(\theta_C-\frac{M_E}{R_{2v}}\times\frac{\theta_C}{\theta_D}\right)-(S_{ii}+S_{ij})\,{}^{\Delta_c}/_{L_{ct}}\right] \tag{16}$$

$$(M_{BG})_{b1}=6\left({}^{EI_{b1}}/_{L_{b1}}\right)\theta_B=6\left({}^{EI_{b1}}/_{L_{b1}}\right)\left(\theta_C-\frac{M_B}{R_{1v}}\right) \tag{17}$$

$$(M_{CH})_{b2}=6\left({}^{EI_{b2}}/_{L_{b2}}\right)\theta_C \tag{18}$$

$$(M_{DI})_{b3}=6\left({}^{EI_{b3}}/_{L_{b3}}\right)\theta_D \tag{19}$$

$$(M_{EJ})_{b4}=6\left({}^{EI_{b4}}/_{L_{b4}}\right)\theta_E=6\left({}^{EI_{b4}}/_{L_{b4}}\right)\left(\theta_D-\frac{M_E}{R_{2v}}\right) \tag{20}$$

Using c_2 as the objective column, the equilibrium of moments at joints C, D, and sway can be calculated using Eqns. 21~23.

$$(M_{BA})_{c1}+(M_{BG})_{b1}+(M_{CH})_{b2}+(M_{CD})_{c2}=0 \tag{21}$$

$$(M_{EF})_{c3}+(M_{EJ})_{b4}+(M_{DI})_{b3}+(M_{DC})_{c2}=0 \tag{22}$$

$$(M_{CD})_{c2}+(M_{DC})_{c2}+P\Delta_c=0 \tag{23}$$

590 Eqn. 23 is used to determine $^{\Delta_c}/_{L_{ct}} = \frac{\mu^2(S_{ii}+S_{ij})(\theta_C+\theta_D)}{-\pi^2+2(S_{ii}+S_{ij})\mu^2}$ by substituting $P = \frac{\pi^2 EI_{c2}}{\mu^2 {L_{c2}}^2}$. By

591 introducing $^{\Delta_c}/_{L_{ct}}$, Eqns. 13~20, relative beam-column stiffness ratios, i.e., $G_{1v} =$

592 $\frac{EI_{b1}/L_{b1}}{EI_{c1}/L_{ct}}, G_{2v} = \frac{EI_{b2}/L_{b2}}{EI_{c2}/L_{ct}}, G_{3v} = \frac{EI_{b3}/L_{b3}}{EI_{c2}/L_{ct}},$ and $G_{4v} = \frac{EI_{b4}/L_{b4}}{EI_{c3}/L_{ct}}$, and IMC-to-column stiffness ratios,

593 i.e., $J_{1v} = \frac{R_{1v}}{EI_{c1}/L_{ct}}, J_{2v} = \frac{R_{1v}}{EI_{c2}/L_{ct}}, J_{3v} = \frac{R_{2v}}{EI_{c2}/L_{ct}},$ and $J_{4v} = \frac{R_{2v}}{EI_{c3}/L_{ct}}$ into Eqns. 21 and 22, Eqns.

594 24 and 25 can be rearranged in the form of ${\theta_C}^2$, ${\theta_D}^2$, and $\theta_C\theta_D$.

$$
\begin{aligned}
&{\theta_C}^2\left[(6G_{1v}+S_{ii})(6G_{2v}+S_{ii})+(6G_{1v}J_{2v}+6G_{2v}J_{1v}+S_{ii}J_{2v}+S_{ii}J_{1v})-\right.\\
&\left.\frac{\mu^2}{-\pi^2+2(S_{ii}+S_{ij})\mu^2}(6G_{1v}+S_{ii}+J_{1v}+J_{2v})\left(S_{ii}+S_{ij}\right)^2\right]+{\theta_D}^2\left[{S_{ij}}^2-\right.\\
&\left.\frac{\mu^2}{-\pi^2+2(S_{ii}+S_{ij})\mu^2}S_{ij}\left(S_{ii}+S_{ij}\right)^2\right]+\theta_C\theta_D\left[S_{ij}(J_{2v}+J_{1v}+6G_{2v}+2S_{ii}+6G_{1v})-\right.\\
&\left.\frac{\mu^2}{-\pi^2+2(S_{ii}+S_{ij})\mu^2}(6G_{1v}+S_{ii}+J_{1v}+J_{2v})\left(S_{ii}+S_{ij}\right)^2-\frac{\mu^2}{-\pi^2+2(S_{ii}+S_{ij})\mu^2}S_{ij}\left(S_{ii}+\right.\right.\\
&\left.\left.S_{ij}\right)^2\right]=0
\end{aligned}
\tag{24}
$$

$$
\begin{aligned}
&{\theta_D}^2\left[(6G_{3v}+S_{ii})(6G_{4v}+S_{ii})+(6G_{4v}J_{3v}+6G_{3v}J_{4v}+S_{ii}J_{4v}+S_{ii}J_{3v})-\right.\\
&\left.\frac{\mu^2}{-\pi^2+2(S_{ii}+S_{ij})\mu^2}(6G_{4v}+S_{ii}+J_{4v}+J_{3v})\left(S_{ii}+S_{ij}\right)^2\right]+{\theta_C}^2\left[{S_{ij}}^2-\right.\\
&\left.\frac{\mu^2}{-\pi^2+2(S_{ii}+S_{ij})\mu^2}S_{ij}\left(S_{ii}+S_{ij}\right)^2\right]+\theta_C\theta_D\left[S_{ij}(J_{3v}+J_{4v}+6G_{3v}+2S_{ii}+6G_{4v})-\right.\\
&\left.\frac{\mu^2}{-\pi^2+2(S_{ii}+S_{ij})\mu^2}(6G_{4v}+S_{ii}+J_{4v}+J_{3v})\left(S_{ii}+S_{ij}\right)^2-\frac{\mu^2}{-\pi^2+2(S_{ii}+S_{ij})\mu^2}S_{ij}\left(S_{ii}+\right.\right.\\
&\left.\left.S_{ij}\right)^2\right]=0
\end{aligned}
\tag{25}
$$

$$
(\theta_C+\beta_1\theta_D)(\beta_2\theta_C+\beta_3\theta_D)=0;\ (\beta_4\theta_C+\theta_D)(\beta_5\theta_C+\beta_6\theta_D)=0 \tag{26}
$$

595 Eqn. 26 is a simplified representation of Eqns. 24 and 25, having four general solutions,

596 i.e., $\begin{vmatrix}1 & \beta_1\\ \beta_4 & 1\end{vmatrix}=0;\ \begin{vmatrix}1 & \beta_1\\ \beta_5 & \beta_6\end{vmatrix}=0;\ \begin{vmatrix}\beta_2 & \beta_3\\ \beta_4 & 1\end{vmatrix}=0;\ \begin{vmatrix}\beta_2 & \beta_3\\ \beta_5 & \beta_6\end{vmatrix}=0$. Eqns. 27~30 provide simplified

597 expressions resulting from solving these general solutions' determinants. The minimum

598 buckling load (P_{cr}/SR) of a sub-assembled CMSF with a rotary IMC, assuming as a

599 semi-rigid IMC, can be obtained by inserting the buckling length (μ) calculated from

600 the maximum value obtained from Eqns. 27~30 into Eqn. 3.

601
$$
1-\left[\frac{2[{S_{ij}}^2-D]}{[S_{ij}(E)-C-D]+\sqrt{[S_{ij}(E)-C-D]^2-4[{S_{ij}}^2-D][A+B-C]}}\right]\left[\frac{2[{S_{ij}}^2-I]}{[S_{ij}J-H-I]+\sqrt{[S_{ij}J-H-I]^2-4[F+G-H][{S_{ij}}^2-I]}}\right]=0 \tag{27}
$$

$$[F+G-H]-\left[\frac{2[{S_{ij}}^2-D]}{[S_{ij}(E)-C-D]+\sqrt{[S_{ij}(E)-C-D]^2-4[{S_{ij}}^2-D][A+B-C]}}\right]\left[\frac{[S_{ij}J-H-I]+\sqrt{[S_{ij}J-H-I]^2-4[F+G-H][{S_{ij}}^2-I]}}{2}\right]=0 \quad (28)$$

$$[A+B-C]-\left[\frac{[S_{ij}(E)-C-D]+\sqrt{[S_{ij}(E)-C-D]^2-4[{S_{ij}}^2-D][A+B-C]}}{2}\right]\left[\frac{2[{S_{ij}}^2-I]}{[S_{ij}J-H-I]+\sqrt{[S_{ij}J-H-I]^2-4[F+G-H][{S_{ij}}^2-I]}}\right]=0 \quad (29)$$

$$[A+B-C][F+G-H]-\left[\frac{[S_{ij}(E)-C-D]+\sqrt{[S_{ij}(E)-C-D]^2-4[{S_{ij}}^2-D][A+B-C]}}{2}\right]\left[\frac{[S_{ij}J-H-I]+\sqrt{[S_{ij}J-H-I]^2-4[F+G-H][{S_{ij}}^2-I]}}{2}\right]=0 \quad (30)$$

Coefficients *A*, *B*, *C*, *D*, *E*, *F*, *G*, and *H* in Eqns. 27~30 are derived from Eqns. 31~34, which are defined in Eqns. 24 and 25 for ${\theta_C}^2$, ${\theta_D}^2$, and $\theta_C\theta_D$. The rotational stiffnesses of rotary IMCs are $R_{1v}=R_{2v}$ =2391.49 kNm/rad, as reported in [26].

$$A=(6G_{1v}+S_{ii})(6G_{2v}+S_{ii});\ B=(6G_{1v}J_{2v}+6G_{2v}J_{1v}+S_{ii}J_{2v}+S_{ii}J_{1v}) \quad (31)$$

$$C=\frac{\mu^2(6G_{1v}+S_{ii}+J_{1v}+J_{2v})(S_{ii}+S_{ij})^2}{-\pi^2+2(S_{ii}+S_{ij})\mu^2};\ D=\frac{\mu^2 S_{ij}(S_{ii}+S_{ij})^2}{-\pi^2+2(S_{ii}+S_{ij})\mu^2} \quad (32)$$

$$E=(J_{2v}+J_{1v}+6G_{2v}+2S_{ii}+6G_{1v});\ F=(6G_{3v}+S_{ii})(6G_{4v}+S_{ii}) \quad (33)$$

$$G=(6G_{4v}J_{3v}+6G_{3v}J_{4v}+S_{ii}J_{4v}+S_{ii}J_{3v});\ H=\frac{\mu^2(6G_{4v}+S_{ii}+J_{4v}+J_{3v})(S_{ii}+S_{ij})^2}{-\pi^2+2(S_{ii}+S_{ij})\mu^2} \quad (34)$$

6.3 Validations

Fig. 22 and **Table 2** compare FEMs' buckling loads (P_{cr}/FE) to theoretical ones (P_{cr}/PD and P_{cr}/SR). The average (Covs) prediction ratios with P_{cr}/PD and P_{cr}/SR are 0.70(0.17) and 0.96(0.09), offering averagely conservative results. However, P_{cr}/PD underestimates findings across a wider range, but P_{cr}/SR minimizes dispersion and produces more accurate results. Despite this, it is still important to account for safety factors due to minor overestimates caused by uncertainties associated with inflection points, semi-rigid behavior, and rotational stiffness. Results indicate that the buckling load prediction of sub-assembled CMSFs could be accurately anticipated by considering rotary IMC's rotational stiffness of $R_{1v}=R_{2v}$ =2391.49 kNm/rad [26]. Alternately, presuming rotary IMC as pinned could not reflect CMSFs' actual compressive behavior and could lead to an uneconomical design. Using pinned assumptions to estimate the buckling load yields conservative values that do not

account for IMCs and apply to all CMSFs. However, sub-assembled CMSF forecasts are more accurate when IMCs are considered semi-rigid. In worst-case scenarios, these equations' conservative nature can impact CMSF design standards. When the other forces acting are small, or the frame has significant rigidity against deformations, these equations can be used to design the dimensions of the members and predict the buckling lengths and loads for CMSF, considering the stiffnesses of its members and IMCs under axial compressions. However, the findings are limited to specific models and require further validation. The outcomes do not apply to non-sway or special frames with welded IMCs or shear-keyed columns. The study's exterior-frame findings can be used to design middle or inner CMSFs by modifying the number of frames.

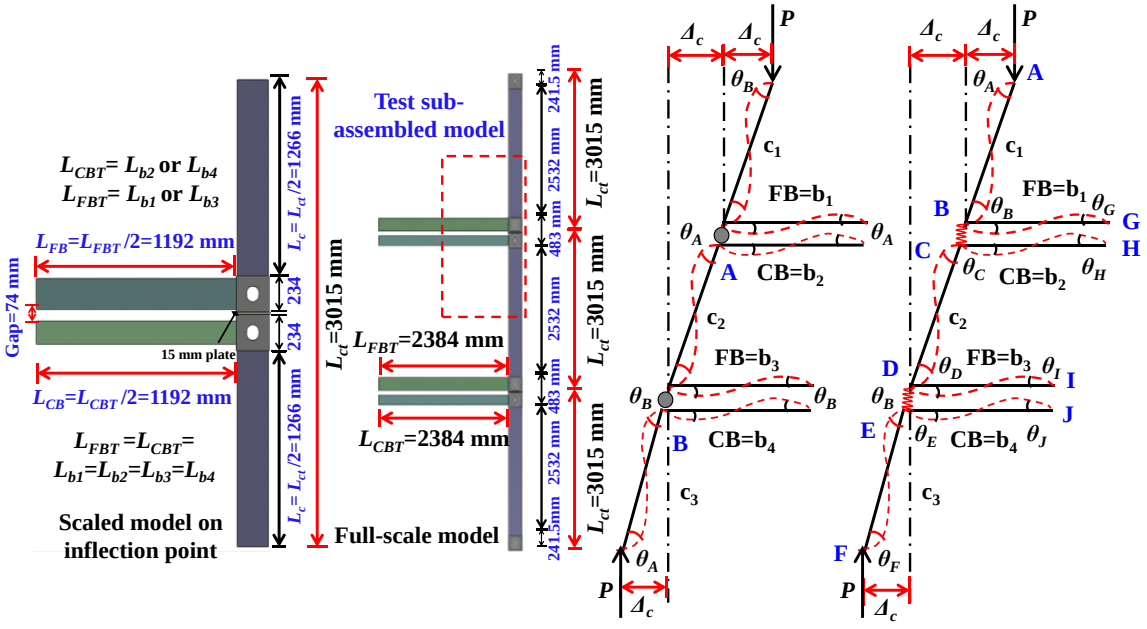

(a) Test sub-assembled model **(b) Three-story model** **(c) Pinned CMSF model** **(d) Semi-rigid CFSM model**

Fig. 21 Theoretical buckling load sub-assembled models; Chen et al.'s model [106] for pinned and Li et al.'s model [99] for semi-rigid CMSFs

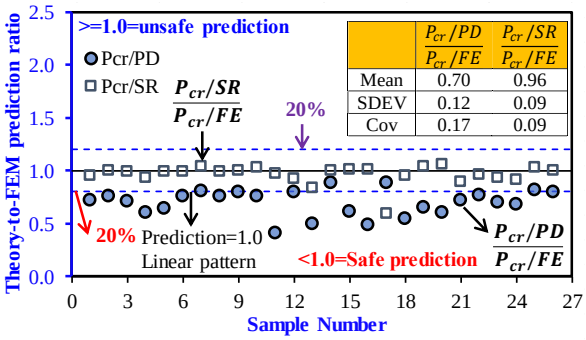

637
638 **Fig. 22** Comparison of Theory-to-FEM

Table 2 Comparison of CMSFs' buckling load via tests-validated FEMs, parametric studies, and theoretical models

Test specimen (#)	P_{cr}/FE (kN)	P_{cr}/PD (kN)	P_{cr}/SR (kN)	$\frac{P_{cr}/PD}{P_{cr}/FE}$	$\frac{P_{cr}/SR}{P_{cr}/FE}$
RS1	1312.5	939.4	1248.3	0.72	0.95
RS2	1342.4	1019.4	1336.6	0.76	1.00
RS3	1241.3	885.6	1234.4	0.71	0.99
Mean				0.73	0.98
Cov				0.03	0.02
FEM (#)	P_{cr}/FE (kN)	P_{cr}/PD (kN)	P_{cr}/SR (kN)	$\frac{P_{cr}/PD}{P_{cr}/FE}$	$\frac{P_{cr}/SR}{P_{cr}/FE}$
SR-1	1304.2	783.6	1210.4	0.60	0.93
SR-2	1321.4	849.9	1302.9	0.64	0.99
SR-3	1514.2	1155.2	1496.1	0.76	0.99
SR-4	1522.0	1228.2	1587.5	0.81	1.04
SR-5	1670.5	1272.4	1659.8	0.76	0.99
SR-6	1670.0	1343.3	1665.1	0.80	1.00
SR-7	1529.9	1157.5	1579.4	0.76	1.03
SR-8	958.9	390.6	932.3	0.41	0.97
SR-9	1888.8	1506.3	1742.0	0.80	0.92
SR-10	1322.0	664.5	1111.9	0.50	0.84
SR-11	1796.5	1599.1	1802.8	0.89	1.00
SR-12	1269.2	770.9	1281.5	0.61	1.01
SR-13	3337.8	1650.7	3386.2	0.49	1.01
SR-26	1353.1	1203.5	801.0	0.89	0.59
SR-28	1829.2	1002.9	1743.4	0.55	0.95
SR-40	1349.1	880.5	1397.5	0.65	1.04
SR-42	1701.8	1019.6	1796.1	0.60	1.06
SR-47	1110.8	801.0	1003.0	0.72	0.90
SR-48	1042.1	801.0	1003.0	0.77	0.96
SR-49	1336.7	939.4	1248.3	0.70	0.93
SR-50	1373.3	939.4	1248.3	0.68	0.91
SR-51	1330.3	1093.8	1376.1	0.82	1.03
SR-52	1372.4	1093.8	1376.1	0.80	1.00
Mean				0.70	0.96
Cov				0.18	0.10

P_{cr}/FE, P_{cr}/PD, and P_{cr}/SR define the buckling load of sub-assembled CMSFs with rotary IMC obtained through experimentally-validated FEMs and theoretical models with pinned and semi-rigid IMCs. *FE* represents the FEM, *PD* denotes the pinned IMC model, and *SR* defines the semi-rigid IMC model.

7 Conclusions

This study comprehensively investigated the compressive behaviors of CMSFs with rotary IMC through sub-assembled tests, parametric FEMs, and theoretical buckling load models. The research yielded the following key findings:

1. The load-shortening behaviors of CMSFs displayed elastic, inelastic, and recessional characteristics. Local buckling occurred on the upper columns initiated from the bending sides to the adjacent faces, resulting in a reduction in capacity, amplified buckling, and apparent sway of the CMSFs.
2. All CMSFs experienced the same failure mode, but the beams' rigidity influenced the direction of sway. Frames and columns tended to sway towards the beams when thinner while bending occurred in the opposite direction when beams were more rigid.
3. The strain curves revealed that only the upper columns had local buckling, either inward or outward, occurring similarly on opposite sides and oppositely on neighboring sides. Elastic buckling developed on columns opposite the bending direction, while plastic buckling occurred on adjacent sides. No failure, buckling, or yielding was noticed in other members and IMCs.
4. Increasing the cross-sectional sizes of beams and columns improved the compressive resistance and rigidity of CMSFs while lengthening members impaired them. Greater member rigidity reduced buckling strain and ductility, causing premature instability.
5. The FEM with a mesh of 30 mm, local imperfection of $H/600$ or $0.64t_c$, and global imperfection of $e=3.35D_c/7$ accurately simulated CMSFs' compression behavior with average prediction errors of 0.3% for P_u.

6. The mean (Cov) theory-to-FEM buckling load for pinned and semi-rigid CMSFs was 0.70(0.17) and 0.96(0.09), indicating that the semi-rigid model provided more precise outcomes with reduced scatter and can accurately predict CMSFs' compressive behavior with rotary IMC.

8 Design recommendations and future research

The extensive research into the compressive behavior of CMSFs with rotary IMCs holds substantial significance for the structural integrity and stability of MSBs, providing valuable insights into modular frame failure modes and capacity. As the results indicate, incorporating rotary IMCs into structural designs necessitates considering the rotational stiffness and behavioral characteristics [17,26]. Meeting performance requirements demand structural members with an appropriate size and stiffness. Parametric studies show that increasing column and beam cross-sectional sizes and thicknesses improves strength; hence, using IMCs with superior geometrical designs could enhance capacity. Moreover, FEMs and theoretical calculations have been verified with experimental and numerical data to estimate buckling loads and failure mechanisms accurately. The complexity and unexpected behavior of IMCs makes designing and analyzing with pinned and rigid assumptions difficult. However, the theoretical models presented in this study provide a systematic classification scheme for pinned and semi-rigid IMCs, enabling interconnection behavior prediction and modular system reliability improvement. Effectively regulating relative stiffnesses based on these models can result in conservative and cost-effective design choices.

Future studies could examine different IMC types' performance to understand their distinct characteristics, potential advantages in multiple applications, and applicability of design models. Using grouped columns, beams, and horizontal and vertical IMCs, middle and interior CMSFs can be studied in modular frame systems. Simplified FEMs

using rotary IMCs spring models could help design multi-story building systems more precisely and efficiently. Such study is essential to MSB development and practical efficacy and safety.

Acknowledgment

The authors acknowledge the National Natural Science Foundation of China for financially supporting their research (Grant No. 51978457 and 52008292). The authors are appreciative of the invaluable suggestions and time spent by the editors and reviewers in enhancing the quality of the paper.

References

[1] Jaillon L, Poon CS. The evolution of prefabricated residential building systems in Hong Kong: A review of the public and the private sector. Autom Constr 2009;18:239–48. https://doi.org/10.1016/j.autcon.2008.09.002.

[2] Liu Y, Chen Z, Liu J, Bai Y, Zhong X, Wang X. Lateral stiffness evaluation on corner-supported thin walled modular steel structures. Thin-Walled Struct 2020;157:106967. https://doi.org/10.1016/j.tws.2020.106967.

[3] Chen LK, Yuan RP, Ji XJ, Lu XY, Xiao J, Tao JB, et al. Modular composite building in urgent emergency engineering projects: A case study of accelerated design and construction of Wuhan Thunder God Mountain/Leishenshan hospital to COVID-19 pandemic. Autom Constr 2021;124:103555. https://doi.org/10.1016/j.autcon.2021.103555.

[4] Chen Z, Khan K, Khan A, Javed K, Liu J. Exploration of the multidirectional stability and response of prefabricated volumetric modular steel structures. J Constr Steel Res 2021;184:106826. https://doi.org/10.1016/j.jcsr.2021.106826.

[5] Corfar D, Tsavdaridis KD. A comprehensive review and classification of inter-module connections for hot-rolled steel modular building systems. J Build Eng 2022;50:104006. https://doi.org/10.1016/j.jobe.2022.104006.

[6] Ferdous W, Bai Y, Duc T, Manalo A, Mendis P. New advancements , challenges and opportunities of multi-storey modular buildings – A state-of-the-art review. Eng Struct 2019;183:883–93. https://doi.org/10.1016/j.engstruct.2019.01.061.

[7] Srisangeerthanan S, Hashemi MJ, Rajeev P, Gad E, Fernando S. Review of performance requirements for inter-module connections in multi-story modular buildings. J Build Eng 2020;28:101087. https://doi.org/10.1016/j.jobe.2019.101087.

[8] Ye Z, Giriunas K, Sezen H, Wu G, Feng D. State-of-the-art review and investigation of structural stability in multi-story modular buildings. J Build Eng 2021;33:101844. https://doi.org/10.1016/j.jobe.2020.101844.

[9] Deng E, Zong L, Ding Y, Zhang Z, Zhang J, Shi F. Seismic performance of mid-to-high rise modular steel construction - A critical review. Thin-Walled Struct 2020;155:106924. https://doi.org/10.1016/j.tws.2020.106924.

[10] Thai H, Ngo T, Uy B. A review on modular construction for high-rise buildings. Structures 2020;28:1265–90. https://doi.org/10.1016/j.istruc.2020.09.070.

[11] Lacey AW, Chen W, Hao H, Bi K. Structural response of modular buildings – An overview. J Build Eng 2018;16:45–56. https://doi.org/10.1016/j.jobe.2017.12.008.

[12] Lawson RM, Ogden RG. "Hybrid" light steel panel and modular systems. Thin-Walled Struct 2008;46:720–30. https://doi.org/10.1016/j.tws.2008.01.042.

[13] Mark Lawson, Ray Odgen CG. Design in Modular Construction Design in Construction. CRC Press Web; 2014.

[14] Lacey AW, Chen W, Hao H. Experimental methods for inter-module joints in modular building structures – A state-of-the-art review. J Build Eng 2022;46:103792. https://doi.org/10.1016/j.jobe.2021.103792.

[15] Shi F, Ding Y, Zong L, Meng X, Chen Y. Axial mechanical behavior of innovative inter-module connection for modular steel constructions. J Build Eng 2023;65:105765. https://doi.org/10.1016/j.jobe.2022.105765.

[16] Dai X, Zong L, Ding Y, Li Z. Experimental study on seismic behavior of a novel plug-in self-lock joint for modular steel construction. Eng Struct 2019;181:143–64. https://doi.org/10.1016/j.engstruct.2018.11.075.

[17] Chen Z, Wang J, Liu J, Cong Z. Tensile and shear performance of rotary inter-module connection for modular steel buildings. J Constr Steel Res 2020;175:106367. https://doi.org/10.1016/j.jcsr.2020.106367.

[18] Yang N, Xia J, Chang H, Zhang L, Yang H. A novel plug-in self-locking inter-module connection for modular steel buildings. Thin-Walled Struct 2023;187:110774. https://doi.org/10.1016/j.tws.2023.110774.

[19] Lacey AW, Chen W, Hao H, Bi K, Tallowin FJ. Shear behaviour of post-tensioned inter-module connection for modular steel buildings. J Constr Steel Res 2019;162:105707. https://doi.org/10.1016/j.jcsr.2019.105707.

[20] Lacey AW, Chen W, Hao H, Bi K. New interlocking inter-module connection for modular steel buildings : Experimental and numerical studies. Eng Struct 2019;198:109465. https://doi.org/10.1016/j.engstruct.2019.109465.

[21] Doh J, Ho NM, Miller D, Peters T, Carlson D, La P. Steel Bracket Connection on Modular Buildings. J Steel Struct Constr 2016. https://doi.org/10.4172/2472-0437.1000121.

[22] Shi F, Ding Y, Zong L, Chen Y, Wu Y. Shear behaviour of vertical inter-module connection with bolts and shear keys for MSCs. Structures 2023;47:260–81. https://doi.org/10.1016/j.istruc.2022.11.046.

[23] Nadeem G, Azizi N, Abu N, Abd I. Evaluation of slip behaviour of self-locking modular steel connection. J Constr Steel Res 2022;197:107467. https://doi.org/10.1016/j.jcsr.2022.107467.

[24] Bazarchi E, Davaran A, Lamarche CP, Roy N, Parent S. Experimental and numerical investigation of a novel vertically unconstrained steel inter-modular connection. Thin-Walled Struct 2023;183:110364. https://doi.org/10.1016/j.tws.2022.110364.

[25] Yu Y, Chen Z, Chen A. Experimental study of a pretensioned connection for modular buildings. Steel Compos Struct 2019;31:217–32. https://doi.org/10.12989/scs.2019.31.3.217.

[26] Chen Z, Liu Y, Zhong X, Liu J. Rotational stiffness of inter-module connection in mid-rise modular steel buildings. Eng Struct 2019;196:109273. https://doi.org/10.1016/j.engstruct.2019.06.009.

[27] Wang Y, Xia J, Ma R, Xu B, Wang T. Experimental Study on the Flexural Behavior of an Innovative Modular Steel Building Connection with Installed Bolts in the Columns. Appl Sci 2019;9:3468. https://doi.org/10.3390/app9173468.

[28] Sanches R, Mercan O, Roberts B. Experimental investigations of vertical post-tensioned connection for modular steel structures. Eng Struct 2018;175:776–89. https://doi.org/10.1016/j.engstruct.2018.08.049.

[29] Chen Z, Liu J, Yu Y. Experimental study on interior connections in modular steel buildings. Eng Struct 2017;147:625–38. https://doi.org/10.1016/j.engstruct.2017.06.002.

[30] Chen Z, Wang J, Liu J, Khan K. Seismic behavior and moment transfer capacity of an innovative self-locking inter-module connection for modular steel building. Eng Struct 2021;245:112978. https://doi.org/10.1016/j.engstruct.2021.112978.

[31] Sanches R, Mercan O. Vertical post-tensioned connection for modular steel buildings. 12th Can. Conf. Earthq. Eng. Quebec City, 2019, p. 1–8.

[32] Lee S, Park J, Shon S, Kang C. Seismic performance evaluation of the ceiling-bracket-type modular joint with various bracket parameters. J Constr Steel Res 2018;150:298–325. https://doi.org/10.1016/j.jcsr.2018.08.008.

[33] Deng E, Zong L, Ding Y, Dai X, Lou N, Chen Y. Monotonic and cyclic response of bolted connections with welded cover plate for modular steel construction. Eng Struct 2018;167:407–19. https://doi.org/10.1016/j.engstruct.2018.04.028.

[34] Chen Z, Liu J, Yu Y, Zhou C, Yan R. Experimental study of an innovative modular steel building connection. J Constr Steel Res 2017;139:69–82. https://doi.org/10.1016/j.jcsr.2017.09.008.

[35] Yang C, Chen H, Ou J. Experimental study on seismic performance of modular steel construction beam-to-beam combined side column joint with blind bolted connection. Thin-Walled Struct 2023;184:110431. https://doi.org/10.1016/j.tws.2022.110431.

[36] Annan CD, Youssef MA, Ei-Naggar MH. Effect of directly welded stringer-to-beam connections on the analysis and design of modular steel building floors. Adv Struct Eng 2009;12:373–83. https://doi.org/10.1260/136943309788708400.

[37] Annan CD, Youssef MA, El Naggar MH. Experimental evaluation of the seismic performance of modular steel-braced frames. Eng Struct 2009;31:1435–46. https://doi.org/10.1016/j.engstruct.2009.02.024.

[38] Annan CD, Youssef MA, El Naggar MH. Seismic vulnerability assessment of modular steel buildings. J Earthq Eng 2009;13:1065–88. https://doi.org/10.1080/13632460902933881.

[39] Annan C, Youssef MA, Naggar MH El, Dean A. Seismic performance of modular steel braced frames. Ninth Can. Conf. Earthq. Eng. Ottawa, Ontario, Canada, 2007. https://doi.org/10.13140/2.1.2132.2241.

[40] Annan C, Youssef MA, Naggar MH El, Dean A. Analytical investigation of semi-rigid floor beams connection in modular steel structures. 33rd Annu. Gen. Conf. Can. Soc. Civ. Eng., 2010. https://doi.org/10.13140/2.1.2010.3687.

[41] Liu J, Chen Z, Liu Y, Bai Y, Zhong X. Full-scale corner-supported modular steel structures with vertical inter-module connections under cyclic loading. J Build Eng 2021;44:103269. https://doi.org/10.1016/j.jobe.2021.103269.

[42] Liu Y, Chen Z, Liu J, Zhong X. Experimental study on seismic behavior of two-storey modular structure. Steel Compos Struct 2020;37:273–89. https://doi.org/10.12989/scs.2020.37.3.273.

[43] Lacey AW, Chen W, Hao H, Bi K. Review of bolted inter-module connections in modular steel buildings. J Build Eng 2019;23:207–19. https://doi.org/10.1016/j.jobe.2019.01.035.

[44] Zhao F, Yu Y, Lin S, Man M. Working mechanism evaluations and simplified models of corner bracket type inter-module connections. Struct Des Tall Spec Build 2021;30:1–21. https://doi.org/10.1002/tal.1858.

[45] Lacey AW, Chen W, Hao H, Bi K. Lateral behaviour of modular steel building with simplified models of new inter-module connections. Eng Struct 2021;236:112103. https://doi.org/10.1016/j.engstruct.2021.112103.

[46] Lyu Y, Li G, Cao K, Zhai S, Wang Y, Mao L. Bending behavior of splice connection for corner-supported steel modular buildings. Eng Struct 2022;250:113460. https://doi.org/10.1016/j.engstruct.2021.113460.

[47] Lyu Y, Li G, Cao K, Zhai S, Li H, Chen C, et al. Behavior of splice connection during transfer of vertical load in full-scale corner-supported modular building. Eng Struct 2021;230:111698. https://doi.org/10.1016/j.engstruct.2020.111698.

[48] Khan K, Chen Z, Liu J, Yan J. Simplified modelling of novel non-welded joints for modular steel buildings. Adv Steel Constr 2021;17:412–24. https://doi.org/10.18057/IJASC.2021.17.4.10.

[49] Khan K, Yan J-B. Finite Element Analysis on Seismic Behaviour of Novel Joint in Prefabricated Modular Steel Building. Int J Steel Struct 2020;20. https://doi.org/10.1007/s13296-020-00320-w.

[50] Nadeem G, Safiee NA, Abu Bakar N, Abd Karim I, Mohd Nasir NA. Finite element analysis of proposed self-locking joint for modular steel structures. Appl Sci 2021;11. https://doi.org/10.3390/app11199277.

[51] Chen H, Ke C, Chen C, Li G. Study on the shear behavior of inter-module connection with a bolt and shear key fi tting for modular steel buildings. Adv Struct Eng 2022;0:1–16. https://doi.org/10.1177/13694332221122547.

[52] Ma R, Xia J, Chang H, Xu B. A component-based model for novel modular connections with inbuild component. Appl Sci 2021;11. https://doi.org/10.3390/app112110503.

[53] Hajimohammadi B, Das S, Ghaednia H, Dhanapal J. Structural performance of registration pin connection in VectorBloc modular construction system. J Constr Steel Res 2022;197:107464. https://doi.org/10.1016/j.jcsr.2022.107464.

[54] Pang S, Yuen J, Liew R, Dai Z. Prefabricated Prefinished Volumetric Construction Joining Techniques Review. 2016 Modul. Offsite Constr. Summit Edmonton, Alberta, Canada, 2016. https://doi.org/10.29173/mocs31.

[55] Shi F, Wang H, Zong L, Ding Y, Su J. Seismic behavior of high-rise modular steel constructions with various module layouts. J Build Eng 2020;31:101396. https://doi.org/10.1016/j.jobe.2020.101396.

[56] Zhang G, Xu L, Xie X. Haunch connecting techniques in a self-centering modular steel structure connection system. J Build Eng 2022;62:105389. https://doi.org/10.1016/j.jobe.2022.105389.

[57] Zhang G, Xu L, Li Z. Experimental evaluation on seismic performance of a novel plug-in modular steel structure connection system. Eng Struct 2022;273:115099. https://doi.org/10.1016/j.engstruct.2022.115099.

[58] Deng E, Yan J, Ding Y, Zong L. Analytical and numerical studies on steel columns with novel connections in Modular Construction. Int J Steel Struct 2017;17. https://doi.org/10.1007/s1329.

[59] Zhang G, Xu L, Li Z. Theoretical and parametric studies of a self-centering modular steel structure connection. Eng Struct 2021;247:113146. https://doi.org/10.1016/j.engstruct.2021.113146.

[60] Ma R, Xia J, Chang H, Xu B, Zhang L. Experimental and numerical investigation of mechanical properties on novel modular connections with superimposed beams. Eng Struct J 2021;232. https://doi.org/10.1016/j.engstruct.2021.111858.

[61] Zhang G, Xu L, Li Z. Development and seismic retrofit of an innovative modular steel structure connection using symmetrical self-centering haunch braces. Eng Struct 2021;229:111671. https://doi.org/10.1016/j.engstruct.2020.111671.

[62] Dai Z, Cheong TYC, Pang SD, Liew JYR. Experimental study of grouted sleeve connections under bending for steel modular buildings. Eng Struct 2021;243:112614. https://doi.org/10.1016/j.engstruct.2021.112614.

[63] Chen Y, Hou C, Peng J. Stability study on tenon-connected SHS and CFST columns in modular construction Stability. Steel Compos Struct 2019;30. https://doi.org/10.12989/scs.2019.30.2.185.

[64] Dai Z, Pang SD, Liew JYR. Axial load resistance of grouted sleeve connection for modular construction. Thin-Walled Struct 2020;154:106883. https://doi.org/10.1016/j.tws.2020.106883.

[65] Khan K, Yan J. Numerical studies on the seismic behaviour of a prefabricated multi-storey modular steel building with new-type bolted joints. Adv Steel Constr 2021;17:1–9. https://doi.org/10.18057/IJASC.2021.17.1.1.

[66] J. Bowron. Locating pin assembly for a modular frame.pdf. WO2020010463A1, 2020.

[67] Chen Z, Li H, Chen A, Yu Y, Wang H. Research on pretensioned modular frame test and simulations. Eng Struct 2017;151:774–87. https://doi.org/10.1016/j.engstruct.2017.08.019.

[68] Peng J, Hou C, Shen L. Lateral resistance of multi-story modular buildings using tenon-connected inter-module connections. J Constr Steel Res 2021;177:106453. https://doi.org/10.1016/j.jcsr.2020.106453.

[69] Peng J, Hou C, Shen L. Numerical simulation of weld fracture using cohesive interface for novel inter-module connections. J Constr Steel Res 2020;174:106302. https://doi.org/10.1016/j.jcsr.2020.106302.

[70] Peng J, Hou C, Shen L. Progressive collapse analysis of corner-supported composite modular buildings. J Build Eng 2022;48:103977. https://doi.org/10.1016/j.jobe.2021.103977.

[71] Peng J, Hou C, Shen L. Numerical analysis of corner-supported composite modular buildings under wind actions. J Constr Steel Res 2021;187:106942. https://doi.org/10.1016/j.jcsr.2021.106942.

[72] Liew JYR, Chua YS, Dai Z. Steel concrete composite systems for modular construction of high-rise buildings. Structures 2019;21:135–49. https://doi.org/10.1016/j.istruc.2019.02.010.

[73] Liew JYR, Chua YS, Dai Z. Steel Concrete Composite Systems for Modular Construction of High-rise Buildings. 12th Int. Conf. Adv. Steel-Concrete Compos. Struct. (ASCCS 2018) Univ. Politècnica València, València, Spain, 2018. https://doi.org/10.4995/ASCCS2018.2018.7220.

[74] Khan K, Chen Z, Liu J, Javed K. State-of-the-Art on Technological Developments and Adaptability of Prefabricated Industrial Steel Buildings. Appl Sci 2023;13.

[75] Srisangeerthanan S, Hashemi MJ, Rajeev P, Gad E, Fernando S. Development of an Innovative Boltless Connection for Multistory Modular Buildings. J Struct Eng 2022;148:1–19. https://doi.org/10.1061/(ASCE)ST.1943-541X.0003382.

[76] Nadeem G, Azizi N, Abu N, Abd I. Experimental and numerical study of self-locking adaptable inter connection for modular steel structures. J Build Eng 2023;65:105723. https://doi.org/10.1016/j.jobe.2022.105723.

[77] Khan K, Chen Z, Liu J, Tsavdaridis KD, Pologanathan K. Axial compression behaviors of steel shear-keyed tubular columns: Numerical and analytical studies. J Constr Steel Res 2023.

[78] Liu Y, Chen Z, Liu J, Zhong X, Liu X, Jiang J. Effects of various reinforcing intra-module connection details on seismic behavior of corner-supported steel modular buildings. Structures 2022;40:555–70. https://doi.org/10.1016/j.istruc.2022.04.041.

[79] CISC. CISC Code of Standard Practice for structural steel. 2016.

[80] JGJ. Technical specification for steel structure of tall building (in Chinese). 2016.

[81] Farajian M, Sharafi P, Kildashti K. The influence of inter-module connections on the effective length of columns in multi-story modular steel frames. J Constr Steel Res 2021;177. https://doi.org/10.1016/j.jcsr.2020.106450.

[82] Ma R, Xia J, Chang H, Xu B, Zhang L. Experimental and numerical investigation of mechanical properties on novel modular connections with superimposed beams. Eng Struct 2021;232. https://doi.org/10.1016/j.engstruct.2021.111858.

[83] Xu B, Xia J, Chang H, Ma R, Zhang L. A comprehensive experimental-numerical investigation on the bending response of laminated double channel beams in modular buildings. Eng Struct 2019;200. https://doi.org/10.1016/j.engstruct.2019.109737.

[84] Xu B, Xia J, Chang H, Ma R, Zhang L. Evaluation of superimposed bending behaviour of laminated channel beams in modular steel buildings subjected to lateral load. Thin-Walled Struct J 2022;175. https://doi.org/10.1016/j.tws.2022.109234.

[85] Wang Q, Su M. Stability study on sway modular steel structures with semi-rigid connections. Thin-Walled Struct 2021;161. https://doi.org/10.1016/j.tws.2021.107529.

[86] Khan K, Chen Z, Liu J, Khan A, Javed K. Axial compression behaviours of tubular sectioned C-shape continuous-supported steel walls in MSB. J Constr Steel Res 2022;188:107009. https://doi.org/10.1016/j.jcsr.2021.107009.

[87] Khan K, Chen Z, Liu J, Khan A. Experimental and numerical study on planar multi-column walls behaviours with boundary supports. J Constr Steel Res 2021;186:106880. https://doi.org/10.1016/j.jcsr.2021.106880.

[88] Khan K, Chen Z, Liu J, Khan A. Numerical and parametric analysis on compressive behaviours of continuous-supported wall systems in MSB. Structures 2021;33:4053–79. https://doi.org/10.1016/j.istruc.2021.07.001.

[89] Hou J, Wang X, Liu J, Chen Z, Zhong X. Study on the stability bearing capacity of multi-column wall in modular steel building. Eng Struct 2020;214:110648. https://doi.org/10.1016/j.engstruct.2020.110648.

[90] Mark Lawson R, Richards J. Modular design for high-rise buildings. Proc Inst Civ Eng Struct Build 2010;163:151–64. https://doi.org/10.1680/stbu.2010.163.3.151.

[91] Khan K, Chen Z, Liu J, Javed K. Compressive behaviors of modular steel shear-keyed grouped tubular columns. J Build Eng 2023;66:105861. https://doi.org/10.1016/j.jobe.2023.105861.

[92] Khan K, Chen Z, Liu J, Javed K. Experimental and analytical investigations on compressive behaviors of modular steel shear-keyed tubes. Eng Struct 2023;279:115604. https://doi.org/10.1016/j.engstruct.2023.115604.

[93] Pengfei Z, Xizhi Z, Zhihua C, Tianxin Z. Design and Mechanical Properties of Multi-storey Steel Module Structure (in Chinese). Tianjin University, 2015.

[94] Dhanapal J, Ghaednia H, Das S, Velocci J. Structural performance of state-of-the-art VectorBloc modular connector under axial loads. Eng Struct 2019;183:496–509. https://doi.org/10.1016/j.engstruct.2019.01.023.

[95] Deng E, Lian J, Zhang Z, Qian H, Zhang G, Zhang P. Axial mechanical behavior of an innovative liftable connection for modular steel construction. Thin-Walled Struct 2023;182:110256. https://doi.org/10.1016/j.tws.2022.110256.

[96] Deng EF, Lian JY, Liu Z, Zhang GC, Wang SB, Cao D Bin. Compressive Behavior of a Fully Prefabricated Liftable Connection for Modular Steel Construction. Buildings 2022;12. https://doi.org/10.3390/buildings12050649.

[97] Wang Q, Su M. Stability study on sway modular steel structures with semi-rigid connections. Thin-Walled Struct 2021;161:107529. https://doi.org/10.1016/j.tws.2021.107529.

[98] Li GQ, Cao K, Lu Y, Jiang J. Effective length factor of columns in non-sway modular steel buildings. Adv Steel Constr 2017;13:412–26. https://doi.org/10.18057/IJASC.2017.13.4.6.

[99] Li GQ, Cao K, Lu Y. Column effective lengths in sway-permitted modular steel-frame buildings. Proc Inst Civ Eng Struct Build 2019;172:30–41. https://doi.org/10.1680/jstbu.17.00006.

[100] Zhai X, Zha X, Chen D. Elastic stability of unbraced plate-type modular steel frames with semi-rigid corner connections. J Constr Steel Res 2022;192:107243. https://doi.org/10.1016/j.jcsr.2022.107243.

[101] Wang Q, Su M. Stability study on sway modular steel structures with semi-rigid connections. Thin-Walled Struct 2021;161:107529. https://doi.org/10.1016/j.tws.2021.107529.

[102] Dumonteil P. Simple Equations for Effective Length Factors. Am Inst Steel Constr 1992;Vol. 29:111–5.

[103] He XHC, Chan TM. Classification system for inter- and intra-module joints in non-sway steel MiC structures. J Constr Steel Res 2023;206:107913. https://doi.org/10.1016/j.jcsr.2023.107913.

[104] Farajian M, Sharafi P, Eslamnia H, Bai Y, Samali B. Classification system for inter-modular connections in non-sway corner-supported steel modular buildings. Structures 2023;49:807–25. https://doi.org/10.1016/j.istruc.2023.01.152.

[105] Farajian M, Sharafi P, Eslamnia H, Kildashti K, Bai Y. Classification of inter-modular connections for stiffness and strength in sway corner-supported steel modular frames. J Constr Steel Res 2022;107458.

[106] Chen Z, Zhong X, Liu Y, Liu J. Analytical and Design Method for the Global Stability of Modular Steel Buildings. Int J Steel Struct 2021;21:1741–58. https://doi.org/10.1007/s13296-021-00532-8.

[107] Fathieh A, Mercan O. Seismic evaluation of modular steel buildings. Eng Struct 2016;122:83–92. https://doi.org/10.1016/j.engstruct.2016.04.054.

[108] Yu Y, Chen Z. Rigidity of corrugated plate sidewalls and its e ff ect on the modular structural design. Eng Struct 2018;175:191–200. https://doi.org/10.1016/j.engstruct.2018.08.039.

[109] Lee S, Park J, Kwak E, Shon S, Kang C, Choi H. Verification of the seismic performance of a rigidly connected modular system depending on the shape and size of the ceiling bracket. Materials (Basel) 2017;10. https://doi.org/10.3390/ma10030263.

[110] L D, Chen W-F. Effective length factor for columns in braced frames. J Struct Eng 1989;114:2357–70.

[111] L. Duan, Chen W-F. Effective length factor for columns in unbraced frames. J Struct Eng 1989;115:149–65.

[112] Sharafi P, Mortazavi M, Samali B, Ronagh H. Interlocking system for enhancing the integrity of multi-storey modular buildings. Autom Constr 2018;85:263–72. https://doi.org/10.1016/j.autcon.2017.10.023.

[113] Chen Z, Zhou Z, Liu J, Ren J, Du E. A kind of corner rotary modular building connection node (in Chinese). CN 106149901 A, 2016.

[114] Xianfeng Li. Tianjin Ziya Shanglinyuan, the first formally approved modular residential project in China (in Chinese). Build Assem Build Netw 2017. https://www.sohu.com/a/143163457_714527.

[115] GB50017-2017. Standard for design of steel structures (in Chinese) 2017.

[116] Zhong X, Chen Z, Liu J, Liu Y, Liu X. Experimental research on the in-plane performance of discontinuous modular diaphragms. Thin-Walled Struct 2022;173:108905. https://doi.org/10.1016/j.tws.2022.108905.

[117] GB/T 228.1-2010. Metallic materials-Tensile testing-Part 1: Method of test at room temperature (in Chinese) 2010.

[118] Liu Y, Chen Z, Liu J, Zhong X, Liu X, Jiang J. Effects of various reinforcing intra-module connection details on seismic behavior of corner-supported steel modular buildings. Structures 2022;40:555–70. https://doi.org/10.1016/j.istruc.2022.04.041.

[119] GBT50344-2019. Technical standards for building structure inspection (in Chinese) 2019.

[120] Sun M, Qu G, Geng L, Hou D, Jing S. Fatigue Properties and Damage Characteristics of Polyurethane Mixtures under a Stress Control Mode. Sustain 2022;14. https://doi.org/10.3390/su141710966.

[121] Wangxi Z. Structural Testing" (Part of the Higher Education Civil Engineering Major Excellent Engineer Education and Training Program Series Planning Textbook)- in Chinese. vol. 2016. 1st ed. Wuhan University Press; 2016.

[122] Yu Y, Lan L, Chen Z, Huang J. Mechanical and seismic behaviors of bottom-flange-bolted upper-flange-welded through-diaphragm connections. J Constr Steel Res 2019;156:86–95. https://doi.org/10.1016/j.jcsr.2019.01.015.

[123] Yan JB, Dong X, Zhu JS. Behaviours of stub steel tubular columns subjected to axial compression at low temperatures. Constr Build Mater 2019;228:116788. https://doi.org/10.1016/j.conbuildmat.2019.116788.

[124] Kang SB, Yang B, Zhou X, Nie SD. Global buckling behaviour of welded Q460GJ steel box columns under axial compression. J Constr Steel Res 2018;140:153–62. https://doi.org/10.1016/j.jcsr.2017.10.013.

[125] Kazemzadeh Azad S, Li D, Uy B. Axial slenderness limits for duplex and lean duplex stainless steel-concrete composite columns. J Constr Steel Res 2020;172:106175. https://doi.org/10.1016/j.jcsr.2020.106175.

[126] Yan J, Zhang B, Yu X, Xie J. Thin-Walled Structures Mechanical properties of stainless steel QN1906Mo at sub-zero temperatures : Tests and stress – strain models. Thin-Walled Struct 2022;179:109727. https://doi.org/10.1016/j.tws.2022.109727.

[127] Yan JB, Luo YL, Liang C, Lin X, Luo YB, Zhang L. Compression behaviours of concrete-filled Q690 high-strength steel tubular columns at low temperatures. J Constr Steel Res 2021;187:106983. https://doi.org/10.1016/j.jcsr.2021.106983.

[128] Yan JB, Yang X, Luo Y, Xie P, Luo YB. Axial compression behaviours of ultra-high performance concrete-filled Q690 high-strength steel tubes at low temperatures. Thin-Walled Struct 2021;169:108419. https://doi.org/10.1016/j.tws.2021.108419.

[129] Yan JB, Wang T, Dong X. Compressive behaviours of circular concrete-filled steel tubes exposed to low-temperature environment. Constr Build Mater 2020;245:118460. https://doi.org/10.1016/j.conbuildmat.2020.118460.

[130] Yan JB, Xie WJ, Luo Y, Wang T. Behaviours of concrete stub columns confined by steel tubes at cold-region low temperatures. J Constr Steel Res 2020;170:106124. https://doi.org/10.1016/j.jcsr.2020.106124.

[131] Yan JB, Dong X, Wang T. Axial compressive behaviours of square CFST stub columns at low temperatures. J Constr Steel Res 2020;164:105812. https://doi.org/10.1016/j.jcsr.2019.105812.

[132] Yan JB, Luo YL, Su L, Lin X, Luo YB, Zhang L. Low-temperature compression behaviour of square CFST columns using Q960 ultra-high strength steel. J Constr Steel Res 2021;183. https://doi.org/10.1016/j.jcsr.2021.106727.

[133] Du Y, Fu M, Chen Z, Yan J, Zheng Z. Axial compressive behavior of CFRP confined rectangular CFT columns using high-strength materials : Numerical analysis and carrying capacity model. Structures 2022;36:997–1020. https://doi.org/10.1016/j.istruc.2021.12.061.

[134] Yan J, Feng J, Luo Y, Du Y. Compression behaviour of stainless-steel stub square tubular columns at cold-region low temperatures. J Constr Steel Res 2021;187:106984. https://doi.org/10.1016/j.jcsr.2021.106984.

[135] ABAQUS (2013). User manual Version 6.13. DS SIMULIA Corp, Provid RI, USA 2013:1–847.

[136] Jia L, Zhao Y, Liu H, Chen Z, Kashan K. Flexural performance of weld-strengthened steel beam-square column joints subjected to axial column loading. J Constr Steel Res 2022;199:107599. https://doi.org/10.1016/j.jcsr.2022.107599.

[137] Gardner L, Saari N, Wang F. Comparative experimental study of hot-rolled and cold-formed rectangular hollow sections. Thin-Walled Struct 2010;48:495–507. https://doi.org/10.1016/j.tws.2010.02.003.

[138] Arrayago I, Rasmussen KJR. Influence of the imperfection direction on the ultimate response of steel frames in advanced analysis. J Constr Steel Res 2022;190:107137. https://doi.org/10.1016/j.jcsr.2022.107137.

[139] Theofanous M, Gardner L. Testing and numerical modelling of lean duplex stainless steel hollow section columns. Eng Struct 2009;31:3047–58. https://doi.org/10.1016/j.engstruct.2009.08.004.

[140] Yan JB, Geng Y, Luo Y, Zhao B, Wang T. Double skin composite beams at Arctic low temperatures: Numerical and analytical studies. J Constr Steel Res 2022;193:107286. https://doi.org/10.1016/j.jcsr.2022.107286.

[141] Yan JB, Dong X, Zhu JS. Behaviours of stub steel tubular columns subjected to axial compression at low temperatures. Constr Build Mater 2019;228. https://doi.org/10.1016/j.conbuildmat.2019.116788.

[142] Yan JB, Feng J, Luo YB, Du Y. Compression behaviour of stainless-steel stub square tubular columns at cold-region low temperatures. J Constr Steel Res 2021;187:106984. https://doi.org/10.1016/j.jcsr.2021.106984.

[143] Zhu J-H, Young B. Cold-Formed-Steel Oval Hollow Sections under Axial Compression. J Struct Eng 2011;137:719–27. https://doi.org/10.1061/(asce)st.1943-541x.0000337.

[144] Dabaon MA, El-Boghdadi MH, Hassanein MF. A comparative experimental study between stiffened and unstiffened stainless steel hollow tubular stub columns. Thin-Walled Struct 2009;47:73–81. https://doi.org/10.1016/j.tws.2008.05.008.

[145] IS 801 - 1975. Indian Standard code of practice for use of cold-formed light gauge steel structural members in general building construction 1975.

[146] IS:800. Indian standard code of practice for general construction in steel. Bur Indian Stand New Delhi 2007.

[147] NZS3404. Part 1:1997-Steel Structures Standard 1997.

[148] EN 1993-1-1. Eurocode 3: Design of steel structures - Part 1-1: General rules and rules for buildings. vol. 1. 2005.

[149] CSA-S16-09. CSA standard-Design of steel structures. vol. 7. 2009.

[150] ANSI/AISC 360-16. AISC360/16 Specification for Structural Steel Buildings-An American National Standard. 2016.

[151] Chen Y, Hou C, Peng J. Stability study on tenon-connected SHS and CFST columns in modular construction. Steel Compos Struct 2019;30:185–99. https://doi.org/10.12989/scs.2019.30.2.185.

[152] Chen WF, Lui EM. Stability design of steel frames. vol. 53. CRC Press; 1991.

1088